Statistics of Matrix Elements of Local Operators in Integrable Models

F. H. L. Essler[1,*] and A. J. J. M. de Klerk[2]

[1]Rudolf Peierls Centre for Theoretical Physics, Clarendon Laboratory, Oxford OX1 3PU, United Kingdom
[2]Institute for Theoretical Physics, University of Amsterdam, Postbus 94485, 1090 GL Amsterdam, The Netherlands

(Received 21 January 2024; accepted 31 July 2024; published 17 September 2024)

We study the statistics of matrix elements of local operators in the basis of energy eigenstates in a paradigmatic, integrable, many-particle quantum theory, the Lieb-Liniger model of bosons with repulsive delta-function interactions. Using methods of quantum integrability, we determine the scaling of matrix elements with system size. As a consequence of the extensive number of conservation laws, the structure of matrix elements is fundamentally different from, and much more intricate than, the predictions of the eigenstate thermalization hypothesis for generic models. We uncover an interesting connection between this structure for local operators in interacting integrable models and the one for local operators that are not local with respect to the elementary excitations in free theories. We find that typical off-diagonal matrix elements $\langle \boldsymbol{\mu}|\mathcal{O}|\boldsymbol{\lambda}\rangle$ in the same macrostate scale as $\exp\left(-c^{\mathcal{O}}L\ln(L)-LM^{\mathcal{O}}_{\boldsymbol{\mu},\boldsymbol{\lambda}}\right)$, where the probability distribution function for $M^{\mathcal{O}}_{\boldsymbol{\mu},\boldsymbol{\lambda}}$ is well described by Fréchet distributions and $c^{\mathcal{O}}$ depends only on macrostate information. In contrast, typical off-diagonal matrix elements between two different macrostates scale as $\exp(-d^{\mathcal{O}}L^2)$, where $d^{\mathcal{O}}$ depends only on macrostate information. Diagonal matrix elements depend only on macrostate information up to finite-size corrections.

DOI: 10.1103/PhysRevX.14.031048 Subject Areas: Quantum Physics, Statistical Physics

I. INTRODUCTION

Fully characterizing the mechanism that underlies the emergence of equilibrium statistical mechanics from the nonequilibrium evolution of many-particle quantum systems has been a long-standing challenge in theoretical physics. A key element of our current understanding is the eigenstate thermalization hypothesis (ETH) [1–4], which relates thermalization in "generic" quantum systems to the statistical properties of matrix elements of (local) operators in energy eigenstates. Here, the term "generic" refers, in particular, to the absence of conservation laws with local densities other than the energy itself. The ETH is a conjecture for the matrix elements $\mathcal{O}_{nm}=\langle n|\mathcal{O}|m\rangle$ in the energy eigenbasis $H|n\rangle=E_n|n\rangle$, and it reads

$$\mathcal{O}_{nm}=O(\bar{E})\delta_{n,m}+e^{-\frac{1}{2}S(\bar{E})}f_{\mathcal{O}}(\bar{E},\omega)R_{nm}. \tag{1}$$

Here, $\bar{E}=(E_n+E_m)/2$, $\omega=E_n-E_m$, $S(\bar{E})$ is the thermodynamic entropy at energy $\bar{E}$, R_{nm} are random variables with zero mean and unit variance, and $O(\bar{E})$ and $f_{\mathcal{O}}(\bar{E},\omega)$ are smooth functions of their arguments. The ETH implies that time averages of observables after a quantum quench from an initial state with subextensive energy fluctuations converge to a steady state, which is equivalent to the microcanonical ensemble. The ETH conjecture is consistent with numerous numerical studies [5–15]. A recent focus has been to clarify the statistical properties of the random variables R_{nm} [16]. By construction, ETH only applies to generic models, and it needs to be modified in the presence of conservation laws. In particular, it clearly does not hold in noninteracting theories, which, in turn, generated significant interest [17–25] in the question of what takes the place of the ETH in integrable models [26–29] that are characterized by having an extensive number of mutually compatible conserved quantities with good spatial locality properties. Curiously, most studies of the statistics of matrix elements in integrable models have not utilized the available analytic results of the structure of these matrix elements [26,30–34], and as a result, they have been restricted to very small system sizes or low particle numbers. This finding, in particular, has precluded a study of how matrix elements scale with system size, which is a serious shortcoming as one is, of course, ultimately interested in understanding how the thermodynamic limit is approached. The purpose of this work is to fully utilize the available information from integrability in order to understand the statistics of matrix elements of local operators in interacting integrable models. We will focus

*Contact author: fab@thphys.ox.ac.uk

on a particular model—the Lieb-Liniger model of bosons with delta-function interactions [26,35]—but we believe our results will carry over to other integrable models. Our choice is based on the following two requirements:

(1) We must be able to compute matrix elements for large systems sizes or particle numbers for energy eigenstates at finite energy densities above the ground state.
(2) We seek an integrable model with free parameters that is equivalent to a noninteracting theory at particular points in parameter space.

Among these requirements, the first point is a much more serious restriction. Almost all integrable models feature hierarchies of multiparticle bound states called "strings" [26–29,36], and it is well understood that the most prevalent (thermal) states at a given energy density involve finite densities of strings. On the one hand, sampling such states in a large finite volume is very challenging; however, more importantly, the corresponding matrix elements become highly singular already for very moderate system sizes, and their numerical evaluation remains an unsolved problem. Thus, for integrable models like the spin-1/2 XXZ chain, matrix elements involving thermal states, i.e., the most likely states at a given energy density, cannot be computed for large system sizes or particle numbers. We avoid this issue by focusing on the repulsive Lieb-Liniger model, where bound states are absent and matrix elements involving thermal states can be readily investigated for large system sizes.

A. Lieb-Liniger model

The Lieb-Liniger model of bosons with δ-function interactions [26,35] is described by the second-quantized Hamiltonian

$$H = \int \mathrm{d}x\big(-\Phi^\dagger(x)\partial_x^2\Phi(x) + c(\Phi^\dagger(x))^2(\Phi(x))^2\big), \quad (2)$$

where $\Phi(x)$ is a complex bosonic field obeying canonical commutation relations

$$[\Phi(x), \Phi^\dagger(y)] = \delta(x-y). \quad (3)$$

The Hamiltonian has a U(1) symmetry related to particle-number conservation, and its first quantized form in the N-particle sector reads

$$\hat{H} = \sum_{j=1}^{N} -\frac{\partial}{\partial x_j^2} + 2c\sum_{i<j}\delta(x_i - x_j). \quad (4)$$

The Lieb-Liniger model is not only a key paradigm for integrable many-particle quantum models [26], but it has also been (approximately) realized in cold atom experiments; see, e.g., the reviews [37,38]. Thus, there has been an intense effort in recent years aimed at understanding dynamical properties of the model both in [33,39–46] and out of equilibrium [47–55].

The outline of this work is as follows. In Sec. II, we briefly review some important properties of energy eigenstates in integrable models. In particular, we introduce the notion of macrostates as families of energy eigenstates characterized by the same densities of the conservation laws, which lies at the heart of our analysis of matrix elements. In Sec. III, we discuss how to efficiently sample energy eigenstates belonging to a given macrostate, which is crucial as the total number of energy eigenstates grows exponentially with the particle number if we impose a momentum cutoff. In Sec. IV, we introduce the operators whose matrix elements we consider in this work, as well as the notion of locality of an operator relative to the elementary excitations of the model considered. In Secs. V and VI, we analyze matrix elements in free theories by considering the example of the impenetrable Bose gas $c = \infty$. While these are simple for operators that are local with respect to the elementary excitations, we reveal an intricate structure of matrix elements of the Bose field, which is the simplest example of a local operator that is not local with respect to the fermionic elementary excitation. In Sec. VII, we then turn to the statistics of matrix elements in the interacting case $0 < c < \infty$ and show that their qualitative behavior is the same as the one we found for the Bose field in the impenetrable limit, i.e., local operator in free theories that are not local with respect to the elementary excitation. We summarize our results in Sec. VIII. Various technical aspects of analytic calculations and methods for sampling eigenstates are presented in two appendixes.

II. ENERGY EIGENSTATES IN INTEGRABLE MODELS

As we are concerned with properties of energy eigenstates in integrable models, we begin by recalling their construction in both free and interacting theories. We draw particular attention to the thermodynamic limit description in terms of macrostates and how these are related to energy eigenstates in very large systems. By virtue of the presence of an extensive number of conservation laws, these have a much more complicated structure than in the generic models to which the ETH applies. Our discussion follows Refs. [56,57].

A. Free theories

Free (noninteracting) theories are the simplest integrable models. In order to be as close as possible to the interacting theory discussed later, we focus on the example of the impenetrable Bose gas [26], i.e., the limit $c \to \infty$ in Eq. (2). This example is well known to be equivalent to a theory of free fermions [58] by the mapping

$$\Phi^\dagger(x) = \Psi^\dagger(x)e^{i\pi\int_{-\infty}^{x} dz\Psi^\dagger(z)\Psi(z)}, \quad (5)$$

where $\Psi(x)$ is a complex fermion field obeying canonical anticommutation relations $\{\Psi(x), \Psi^\dagger(y)\} = \delta(x-y)$. The second-quantized Hamiltonian then becomes block-diagonal in the sectors with even or odd fermion number, and each block takes the simple form

$$H(\infty) = -\int dx\, \Psi^\dagger(x)\partial_x^2\Psi(x). \tag{6}$$

The wave functions of energy eigenstates of the bosonic and fermionic realizations are related by the celebrated Girardeau formula [59]

$$\chi_F(z_1,\ldots,z_N) = \prod_{i<j}\mathrm{sgn}(z_j - z_i)\chi_B(z_1,\ldots,z_N). \tag{7}$$

Having in mind this simple relationship, we will therefore focus on the construction of energy eigenstates in the free fermion representation. The Hamiltonian on a ring of circumference L is diagonalized by going to Fourier space,

$$H(\infty) = \sum_p p^2\Psi_p^\dagger\Psi_p, \tag{8}$$

where $p = 2\pi I_n/L$, with I_n half-odd integers (integers) in the sector with even (odd) fermion number and

$$\Psi_p = \frac{1}{\sqrt{L}}\int_0^L dx\, e^{-ipx}\Psi(x). \tag{9}$$

There is an extensive number of mutually compatible conservation laws with local densities

$$Q^{(n)} = \sum_p p^n\Psi_p^\dagger\Psi_p, \qquad [Q^{(n)}, Q^{(m)}] = 0. \tag{10}$$

A complete set of simultaneous N-particle eigenstates of all the $Q^{(n)}$ is given by the momentum-space Fock states

$$|\boldsymbol{p}\rangle = \prod_{j=1}^N \Psi_{p_j}^\dagger|0\rangle, \qquad p_1 < p_2 \cdots < p_N, \tag{11}$$

which have eigenvalues

$$Q^{(n)}|\boldsymbol{p}\rangle = \sum_{j=1}^N p_j^n|\boldsymbol{p}\rangle. \tag{12}$$

1. Macrostates

Local properties in the thermodynamic limit

$$N, L \to \infty, \qquad D = \frac{N}{L} \text{ fixed} \tag{13}$$

are conveniently described in terms of macrostates. These families of energy eigenstates have the same local properties. The latter are, in turn, fully encoded in the extensive parts of the eigenvalues (12) of the conservation laws. These observations lead us to consider families of Fock states $\{|k_1,\ldots,k_N\rangle\}$ for asymptotically large L and $N = DL$, which are characterized by a positive function $0 \le \rho(k) \le (1/2\pi)$ termed the root density through

$$L\rho(k)\Delta k = \text{number of } k_j \text{ in } [k, k+\Delta k]. \tag{14}$$

It is then straightforward to see that any microstate $\{|k_1,\ldots,k_N\rangle\}$ associated with the same root density $\rho(\lambda)$ has the same extensive parts of the eigenvalues (12) of the conservation laws $Q^{(n)}$,

$$\frac{1}{L}\sum_{j=1}^N k_j^n = \int_{-\infty}^{\infty} dk\,\rho(k)k^n + o(L^0). \tag{15}$$

(a) *Counting microstates.* For a given $\rho(k)$, there are generally exponentially many (in the system size L) eigenstates satisfying Eq. (14). In the interval $[k, k+\Delta k]$, a momentum k_j can take $\Delta n_{\mathrm{vac}} = \lfloor L\Delta k/2\pi\rfloor$ possible values (here, $\lfloor x\rfloor$ denotes the integer part of x). The root density determines how many of these "vacancies" (possible values) are occupied, with the occupation number given by $\Delta n_{\mathrm{p}} = \lfloor\rho(k)L\Delta k\rfloor$. The Δn_{p} occupied momenta can be distributed over the Δn_{vac} vacancies in $C(\Delta n_{\mathrm{vac}}, \Delta n_{\mathrm{p}})$ possible ways, where $C(n,m)$ denotes a binomial coefficient. The entropy of our macrostates is given by $S = \ln(\#\text{ of microstates})$, where reordering of momenta in a given interval $[k, k+\Delta k]$ contributes $\Delta S = \ln[C(\Delta n_{\mathrm{vac}}, \Delta n_{\mathrm{p}})]$. Using Stirling's approximation under the assumption that Δn_{vac} and Δn_p scale with L, we then have, in the large volume limit,

$$S[\rho] = s[\rho]L = L\int_{-\infty}^{\infty} \mathrm{d}k[(\rho(k)+\rho_h(k))\ln(\rho(k)+\rho_h(k)) - \rho(k)\ln(\rho(k)) - \rho_h(k)\ln(\rho_h(k))] + o(L). \tag{16}$$

Here, we have defined a hole density by

$$\rho_h(k) = \frac{1}{2\pi} - \rho(k). \tag{17}$$

(b) *Typical vs atypical states.* Let us consider energy eigenstates at energy density e and particle density D. Clearly, there will be infinitely many macrostates satisfying these conditions: All we require is a positive function $\rho(k)$ such that

$$e = \int_{-\infty}^{\infty} dk\rho(k)k^2, \qquad D = \int_{-\infty}^{\infty} dk\rho(k). \tag{18}$$

Generically, these macrostates will have finite entropy densities in the thermodynamic limit [see Eq. (16)], and importantly, they will generally not be thermal. Indeed, thermal macrostates are obtained by minimizing the free energy per site:

$$f[\rho] = \int_{-\infty}^{\infty} \mathrm{d}k(k^2 - \mu)\rho(k) - Ts[\rho], \tag{19}$$

where μ is a chemical potential that determines D. This process leads to the root density taking the form of a Fermi distribution at temperature T,

$$\frac{\delta f[\rho]}{\delta\rho(k)} = 0 \Rightarrow \rho_{\mathrm{th}}(k) = \frac{1}{2\pi}\frac{1}{e^{(k^2-\mu)/T}+1}. \tag{20}$$

Fixing the chemical potential and temperature by inserting Eq. (20) into Eq. (18) provides us with a root density of thermal states. By construction, thermal states are maximal entropy states for given e and D; i.e., they are the most likely states. As we have seen above, other macrostates will exist at the same energy density with entropies that are smaller than those of the thermal state. If at a given energy density we select a microstate at random, it will be thermal, with a probability that is exponentially close (in system size) to one. We call such states "typical," while noting that there are exponentially many microstates that are "atypical," which differ from thermal microstates in the values of the higher conservation laws $Q^{(n)}$ and hence have different local properties (as the densities of $Q^{(n)}$ are local operators and macrostates are homogeneous).

The situation with typical and atypical microstates generalizes to the case of integrable models with interactions [56], and atypical states within these models can have very interesting properties (see, for example, Refs. [52,60,61]).

B. Interacting theories: Lieb-Liniger model at $0 < c < \infty$

The Lieb-Liniger model is famously solvable by a coordinate Bethe ansatz [35], and we now briefly summarize the key steps following Ref. [26]. The eigenvalue equation for the first quantized Hamiltonian (4) reads

$$\hat{H}\chi(x_1,\ldots,x_N) = E\chi(x_1,\ldots,x_N), \tag{21}$$

where the wave functions fulfill periodic boundary conditions

$$\chi_{\boldsymbol{\lambda}}(x_1,\ldots,x_j+L,x_N) = \chi_{\boldsymbol{\lambda}}(x_1,\ldots x_N). \tag{22}$$

The (unnormalized) solutions take the Bethe ansatz form

$$\chi_{\boldsymbol{\lambda}}(x_1,\ldots x_N) = \sum_{P\in S_N}\mathrm{sgn}(P)e^{i\sum_{j=1}^{N}\lambda_{P_j}x_j} \times\prod_{j>k}[\lambda_{P_j}-\lambda_{P_k}-ic], \tag{23}$$

where the rapidities $\boldsymbol{\lambda} = \{\lambda_1,\ldots,\lambda_N\}$ satisfy nontrivial quantization conditions known as Bethe equations,

$$e^{i\lambda_j L} = -\prod_{k=1}^{N}\frac{\lambda_j-\lambda_k+ic}{\lambda_j-\lambda_k-ic}, \quad j=1,\ldots,N. \tag{24}$$

The energy and momentum eigenvalues of these states are

$$E_{\boldsymbol{\lambda}} = \sum_{j=1}^{N}\lambda_j^2, \qquad P_{\boldsymbol{\mu}} = \sum_{j=1}^{N}\lambda_j. \tag{25}$$

The states are, in fact, simultaneous eigenstates of an infinite number of mutually compatible higher conservation laws $Q^{(n)}$ [26,62],

$$Q^{(n)}\chi_{\boldsymbol{\lambda}}(x_1,\ldots,x_N) = \nu_{\boldsymbol{\lambda}}^{(n)}\chi_{\boldsymbol{\lambda}}(x_1,\ldots,x_N), \qquad \nu_{\boldsymbol{\lambda}}^{(n)} = \sum_{j=1}^{N}\lambda_j^n. \tag{26}$$

In practice, we will use the set of equations known as the logarithmic Bethe equations, which are obtained by taking the logarithm of Eq. (24):

$$\lambda_j L + \sum_{k=1}^{N}\theta(\lambda_j-\lambda_k) = 2\pi I_j, \qquad \theta(x) = 2\arctan\left(\frac{x}{c}\right). \tag{27}$$

In taking the logarithm, we introduce I_j, which is an integer (half-odd integer) for N odd (even). Each solution of the Bethe equations (24) is in one-to-one correspondence with a set of distinct (half-odd) integers $\{I_j\}$, and hence the set of distinct integers defines a wave function $\chi_{\boldsymbol{\lambda}}(x_1,\ldots,x_N)$ that is a simultaneous eigenstate of the Hamiltonian and the conservation laws.

1. Solutions of the Bethe equations

An important simplification that occurs for the Lieb-Liniger model is that all solutions to the Bethe equations are in fact real [26]. This finding greatly simplifies the task of solving the Bethe equations numerically. In other interacting integrable models, the solutions are typically complex and form regular patterns known as "strings" [27,28]. As noted above, solutions of the Bethe equations involving strings are numerically very difficult to obtain because some of the differences between the corresponding rapidities lie exponentially (in system size) close to poles of the Bethe equations.

2. Macrostates

Given the above description of energy eigenstates in terms of the solutions of the Bethe equations, we now turn to the construction of macrostates. The main complication here, as compared to the process for the free theory (described in Sec. II A 1), is that the quantization conditions described in Eqs. (24) and (27) are nontrivial, so the set of rapidities $\boldsymbol{\lambda}$ are state dependent. However, we can avoid this complication by instead working with the (half-odd) integers $\{I_j\}$—in analogy with Eq. (14), we can define a density for $\nu_j = I_j/L$ through

$$L\varrho(\nu)\Delta\nu = \text{number of } \frac{I_j}{L} \text{ in } [\nu, \nu+\Delta\nu]. \tag{28}$$

As in the free theory, a positive function $\varrho(\nu)$ specifies a macrostate, and corresponding microstates can be constructed by choosing $\{I_j\}$ distributed according to $\varrho(\nu)$. In practice, it is useful to have a formulation in terms of the distribution function $\rho(\lambda)$—called root density—of the rapidities λ_j that satisfy Eq. (24), defined via

$$L\rho(\lambda)\Delta\lambda = \text{number of } \lambda_j \text{ in } [\lambda, \lambda+\Delta\lambda]. \tag{29}$$

The relationship between $\rho(\lambda)$ and $\varrho(\nu)$ can be obtained from Eq. (27) by converting the sum over rapidities to an integral over $\rho(\lambda)$ in the thermodynamic limit

$$\begin{aligned} z_j = \frac{I_j}{L} &= \frac{\lambda_j}{2\pi} + \frac{1}{2\pi L}\sum_{k=1}^{N}\theta(\lambda_j-\lambda_k) \\ &\simeq \frac{\lambda_j}{2\pi} + \frac{1}{2\pi}\int_{-\infty}^{\infty} \mathrm{d}\mu\, \theta(\lambda_j-\mu)\rho(\mu). \end{aligned} \tag{30}$$

Thus, in the thermodynamic limit, we have

$$z(\lambda) = \frac{\lambda}{2\pi} + \frac{1}{2\pi}\int_{-\infty}^{\infty} \mathrm{d}\mu\, \theta(\lambda-\mu)\rho(\mu). \tag{31}$$

The strictly monotonically increasing function $z(\lambda)$ is known as the counting function. It is useful to define a so-called hole density $\rho_h(\lambda)$ associated with a macrostate by taking the derivative of Eq. (31),

$$\rho(\lambda) + \rho_h(\lambda) = \frac{1}{2\pi} + \int \frac{d\mu}{2\pi} K(\lambda-\mu)\rho(\mu), \tag{32}$$

$$K(\lambda) = \frac{2c}{c^2+\lambda^2}. \tag{33}$$

The relationship between $\varrho(z)$ and $\rho(\lambda)$ is obtained by equating the number of rapidities and integers within each interval $d\lambda$,

$$\varrho(\nu) = \rho\big(\lambda(\nu)\big)\frac{d\lambda}{d\nu}. \tag{34}$$

Given that $\nu = z\big(\lambda(\nu)\big)$, we have

$$\frac{dz}{d\nu} = 1 = \frac{dz}{d\lambda}\frac{d\lambda}{d\nu} = \big(\rho(\lambda)+\rho_h(\lambda)\big)\frac{d\lambda}{d\nu}, \tag{35}$$

and hence

$$\varrho(\nu) = \frac{\rho(\lambda)}{\rho(\lambda)+\rho_h(\lambda)} = \frac{1}{1+\frac{\rho_h(z^{-1}(\nu))}{\rho(z^{-1}(\nu))}}. \tag{36}$$

3. Thermal macrostates

Thermal macrostates are obtained by maximizing the entropy for fixed energy and particle densities [27]. The entropy density is given by the same expression (16) as in the noninteracting case, with the important proviso that $\rho_h(\lambda)$ is now obtained from Eq. (32). Extremizing the entropy for fixed energy and particle densities fixes the corresponding root density in terms of the (nonlinear) integral equations,

$$\begin{aligned} \rho(\lambda) &= \frac{1}{2\pi(1+e^{\frac{\epsilon(\lambda)}{T}})} + \int_{-\infty}^{\infty} d\mu \frac{K(\lambda-\mu)}{2\pi(1+e^{\frac{\epsilon(\lambda)}{T}})}\rho(\mu), \\ \epsilon(\lambda) &= \lambda^2 - h - \frac{T}{2\pi}\int d\mu K(\lambda-\mu)\ln\left[1-e^{-\frac{\epsilon(\mu)}{T}}\right]. \end{aligned} \tag{37}$$

Here, T is the temperature, and h is a chemical potential that fixes the particle density. The corresponding function $\varrho(\nu)$ is obtained by determining $z(\lambda)$ from Eq. (31), and then using Eq. (36),

$$\varrho(\nu) = \frac{1}{1+e^{\epsilon(z^{-1}(\nu))/T}}. \tag{38}$$

III. GENERATING MICROSTATES FOR A GIVEN MACROSTATE

We now turn to the problem of generating microstates (in a large but finite system) associated with a macrostate characterized by a root density $\rho(x)$ in the thermodynamic limit. We start our discussion by considering what we call smooth microstates of N particles in a system of size L. Let us assume, for definiteness, that our state is characterized by half-odd integers I_j. We define a "particle counting function" by

$$z_p(x) = \int_{-\infty}^{x} dy \rho(y), \tag{39}$$

and then numerically solve the equations

$$z_p(\lambda_j^{(0)}) = \frac{j}{L}, \quad j = 1, 2, \ldots, N. \tag{40}$$

This method provides us with a set $\{\lambda_j^{(0)}\}$ of rapidities, from which we generate a set of half-odd integers I_j as

$$I_j = L \ \mathrm{Round}(z(\lambda_j^{(0)})) + \frac{1}{2}\mathrm{sgn}(z(\lambda_j^{(0)})), \tag{41}$$

where $z(\lambda)$ is the counting function in the thermodynamic limit defined in Eq. (31). Having determined our set of half-odd integers $\{I_1, \ldots, I_N\}$, we then obtain the corresponding rapidities for a system of size L by numerically solving the logarithmic form of the Bethe equations (27). The histogram of the corresponding integers or rapidities is, by construction, fairly smooth and closely tracks the thermodynamic root density. An example in the particularly simple case $c = \infty$ is shown in Fig. 1. The rationale behind considering this state is that it can be scaled up in system size, which will allow us to consider the probability distribution function (PDF) of matrix elements between the smooth state and energy eigenstates belonging to the same or another macrostate.

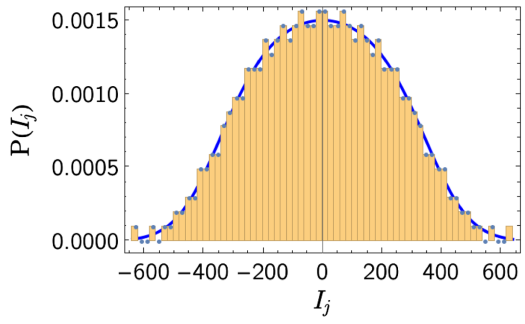

FIG. 1. Normalized histogram for the distribution of integers for $L = N = 512$ and the smooth microstate corresponding to a thermal macrostate with $c = \infty$, $\beta = 0.1$, and $D = 1$.

A. Sampling microstates for a given macrostate

As we are interested in statistical properties of matrix elements of local operators between energy eigenstates, we require a method for randomly sampling given classes of eigenstates. This method is a necessity because the number of microstates corresponding to a given macrostate grows extremely rapidly with system size, cf. the discussion in Sec. II. The basic principle is to sample the (half-odd) integers I_j that specify micro-states in such a way that they are distributed according to the distribution function $\varrho(\nu)$ that defines the macrostate of interest. The difficulty is knowing how close the resulting histogram for a finite system of a few hundred particles should be to the thermodynamic limit distribution $\varrho(\nu)$ in order for a microstate characterized by a set $\{I_j\}$ to "belong" to the macrostate defined by $\varrho(\nu)$. A detailed discussion of this issue and its resolution is given in Appendix B. The upshot is that we employ the following "simplified random sampling" algorithm:

(1) Introduce a cutoff $I_{\max}$, and define a set of (half-odd) integers $\mathfrak{S} = \{-I_{\max}, -I_{\max}+1, \ldots, I_{\max}\}$ and an empty set S.
(2) Impose that the I_j are distributed according to a PDF $P(\nu)$.
(3) Determine the inverse $Z^{-1}(\nu)$ of the cumulative distribution function,

$$Z(\nu) = \int_0^{\nu} d\nu' P(\nu'), \qquad -\frac{1}{2} \le Z(\nu) \le \frac{1}{2}. \tag{42}$$

(4) Generate a random number $|r| \le \frac{1}{2}$, and use it to generate a random integer

$$I = \mathrm{Round}(LZ^{-1}(r)). \tag{43}$$

(5) Then, update the sets $\mathfrak{S}$ and S according to the rule

$$\text{If } I \in \mathfrak{S} \wedge I \notin S \quad \text{then } S \to S \cup \{I\}, \qquad \mathfrak{S} \to \mathfrak{S} - \{I\}. \tag{44}$$

(6) Repeat steps 4 and 5 until we arrive at a set $\{I_1, \ldots, I_N\}$ of distinct integers.

The PDF $P(\nu)$ is chosen such that this random sampling process *on average* reproduces the thermodynamic distribution $\varrho(\nu)$, which can be achieved through an iterative numerical procedure. We show the resulting PDF for $T = 10$, $D = 1$, and $c = \infty$ in Fig. 2.

IV. LOCAL OPERATORS

Some representative, spatially local operators in the Lieb-Liniger model are as follows:

(i) Density operator,

$$\rho(x) = \Phi^\dagger(x)\Phi(x). \tag{45}$$

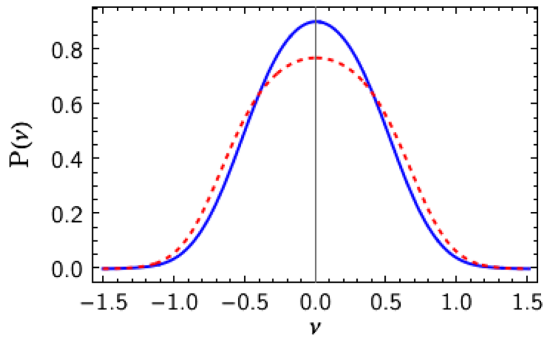

FIG. 2. PDF $P(\nu)$ (solid blue line) and $\varrho(\nu)$ (dashed red line) for $T = 10$, $D = 1$, and $c = \infty$.

(ii) Interaction,

$$g_2(x) = (\Phi^\dagger(x))^2(\Phi(x))^2. \tag{46}$$

(iii) Bose field,

$$\Phi(x). \tag{47}$$

As discussed earlier, in the limit $c \to \infty$, the model becomes equivalent to free fermions, and in this limit, additional local operators become of interest:

(i) Fermi field at $c = \infty$,

$$\Psi^\dagger(x) = \Phi^\dagger(x)e^{i\pi\int_{-\infty}^{x} dz\Phi^\dagger(z)\Phi(z)}. \tag{48}$$

(ii) Operator products involving the Fermi field at $c = \infty$, e.g.,

$$\begin{aligned} J_n(x) &= (-i)^n\Psi^\dagger(x)\partial_x^n\Psi(x), \\ F_n^\dagger(x) &= \Psi^\dagger(x)(\partial_x^n\Psi^\dagger(x))\Psi(x). \end{aligned} \tag{49}$$

All of the above operators are, by construction, spatially local (for finite values of n). However, in integrable models, the existence of stable particle and hole excitations (at all energy densities) leads to an additional notion of locality. The stable excitations themselves have good spatial locality properties in the sense that they represent a local disturbance of the macrostate under consideration. It is then natural to ask whether a given local operator, say, $\hat{\rho}(x)$, is local with respect to the operator that creates a local stable excitation. In relativistic integrable QFTs (at zero density), related notions of locality are known to have far-reaching consequences for matrix elements of local operators between energy eigenstates [30,63].

In the impenetrable limit, the situation becomes particularly simple. Here, the elementary excitations are fermions, and they are created by $\Psi^\dagger(x)$. Operators like $\rho(x)$, $g_2(x)$, $J_n(x)$, and, of course, also $\Psi^\dagger(x)$ itself are local relative to $\Psi^\dagger(x)$ and, in particular, (anti)commute at a distance. On the other hand, the Bose field itself is not local relative to $\Psi^\dagger(x)$ as it involves a Jordan-Wigner-like string operator. As is discussed below, this fact leads to a dramatic difference in the structure of matrix elements in energy eigenstates.

V. DIAGONAL MATRIX ELEMENTS OF LOCAL OPERATORS IN FREE THEORIES

We first consider matrix elements of local operators in noninteracting theories. The naive expectation might be that they are trivial, but as we will see, this is not the case for operators that are not local with respect to the elementary excitations. At $c = \infty$, energy eigenstates can be expressed as fermionic Fock states. Given a macrostate described by a root density $\rho(k)$, we can construct a corresponding microstate $|\boldsymbol{k}\rangle = |k_1, \ldots, k_N\rangle$ following the procedure outlined in Sec. III. Expectation values of local operators can then be straightforwardly calculated. Let us start with the single-fermion Green's function at a fixed separation $x - y = \mathcal{O}(L^0)$,

$$\begin{aligned} \langle \boldsymbol{k}|\Psi^\dagger(x)\Psi(y)|\boldsymbol{k}\rangle &= \frac{1}{L}\sum_{p,q}\langle \boldsymbol{k}|\Psi_p^\dagger\Psi_q|\boldsymbol{k}\rangle e^{iyq-ipx} \\ &= \int_{-\infty}^{\infty} dk e^{ik(y-x)}\rho(k) + o(L^0). \end{aligned} \tag{50}$$

Importantly, up to finite-size corrections, this expectation value only depends on the root density $\rho(k)$ characterizing the macrostate of interest. It is straightforward to extend this calculation to more complicated expectation values of the form

$$\langle \boldsymbol{k}|\Psi^\dagger(x_1)\ldots\Psi^\dagger(x_n)\Psi(y_n)\ldots\Psi(y_1)|\boldsymbol{k}\rangle, \tag{51}$$

where we take n to be fixed and all x_j and all y_ℓ to lie in an interval of fixed size $\mathcal{O}(L^0)$. Applying Wick's theorem and using Eq. (50), we conclude that expectation values of any multipoint correlation function involving a fixed, finite number of fermion operators on a finite interval can be expressed solely in terms of the macrostate, up to finite-size corrections. It then follows in turn that expectation values of any finite number of fermion operators calculated between different microstates corresponding to the same macrostate differ only by finite-size corrections that go to zero in the thermodynamic limit. Expectation values of local operators involving the Bose field at $c = \infty$, such as

$$\langle \boldsymbol{k}|\Phi^\dagger(x)\partial_x\Phi(x)|\boldsymbol{k}\rangle, \tag{52}$$

can be obtained from these results by using the Bose-Fermi mapping, as the latter involves only a finite number of Fermi fields. This case is in contrast to expectation values like

$$\langle \boldsymbol{k}|\Phi^\dagger(x)\Phi(y)|\boldsymbol{k}\rangle = \langle \boldsymbol{k}|\Psi^\dagger(x)e^{i\pi\int_y^x dz\Psi^\dagger(z)\Psi(z)}\Psi(y)|\boldsymbol{k}\rangle, \tag{53}$$

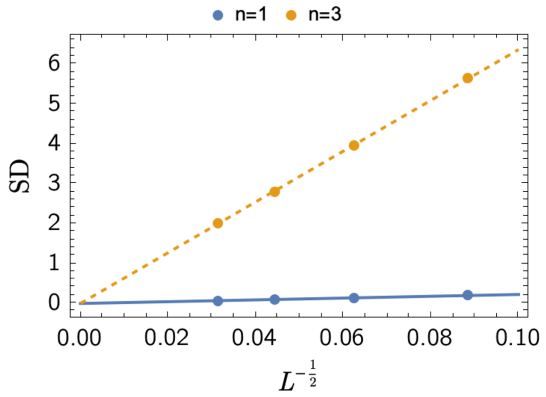

FIG. 3. Standard deviations of the PDFs $P(\mathfrak{J}_n(\boldsymbol{k}))$ for $n = 1, 3$ and thermal microstates $|\boldsymbol{k}\rangle$ at $T = 10$, $D = 1$ sampled in a microcanonical window $|E - e_\infty L| < 10$.

which can no longer be evaluated by using Wick's theorem for a finite number of Fermi fields. This finding is intimately related to the fact that the Bose and Fermi fields are not mutually local. In order to assess how quickly the diagonal matrix elements approach their thermodynamic value with increasing L, we have considered the expectation values of the operators $J_n(0)$ [Eq. (49)] for $n = 1, 3$ in thermal microstates $|\boldsymbol{k}\rangle$ at temperature $T = 10$ and density $D = 1$,

$$\mathfrak{J}_n(\boldsymbol{k}) = \langle \boldsymbol{k}|J_n(0)|\boldsymbol{k}\rangle. \tag{54}$$

We determine the PDF of $\mathfrak{J}_n(\boldsymbol{k})$ when the thermal microstates $|\boldsymbol{k}\rangle$ are sampled in a microcanonical window $|E - e_\infty L| < 10$, where e_∞ is the thermal energy density in the thermodynamic limit and E the energy eigenvalue of the microstate. The PDFs are well described by normal distributions, and their standard deviations as functions of system size are shown in Fig. 3. As the data are well described by simple linear fits, we conclude that the standard deviations scale to zero as $L^{-1/2}$. This finding is in agreement with results on free theories in the literature [21].

VI. OFF-DIAGONAL MATRIX ELEMENTS IN FREE THEORIES

Our example for a free theory is again the $c = \infty$ limit of the Lieb-Liniger model. As we will see, the structure of off-diagonal matrix elements depends strongly on the locality properties of local operators $\mathcal{O}$ relative to the Fermi field Ψ. As before, we consider N particles on a ring of length L and are interested in the thermodynamic limit $N, L \to \infty$ at fixed $D = N/L$.

A. Local operators that are local relative to the Fermi field

The density operator $\rho(x)$ is spatially local as well as local with respect to the elementary fermion excitations of the Lieb-Liniger model at $c = \infty$. Let $|\boldsymbol{\lambda}\rangle$, $|\boldsymbol{\mu}\rangle$ be energy eigenstates with corresponding sets of (half-odd) integers $\{I_j\}$ and $\{J_k\}$. The matrix elements of the density operator vanish unless $\{I_j\}$ and $\{J_k\}$ differ by precisely one particle-hole excitation

$$\forall\, j \neq a \quad I_j = J_j, \quad J_a = I_a + n \notin \{I_j\}. \tag{55}$$

For such one-particle-hole excitations, we have the simple result

$$\left.\frac{|\langle \boldsymbol{\mu}|\rho(0)|\boldsymbol{\lambda}\rangle|^2}{\langle \boldsymbol{\lambda}|\boldsymbol{\lambda}\rangle\langle \boldsymbol{\mu}|\boldsymbol{\mu}\rangle}\right|_{\text{1ph}} = \frac{1}{L^2}. \tag{56}$$

If we introduce a cutoff Λ in momentum, the total number N_{ph} of states $|\boldsymbol{\mu}\rangle$ that lead to nonvanishing off-diagonal matrix elements scales polynomially with system size,

$$N_{\text{ph}} = N\left(\frac{2L\Lambda}{2\pi} - N\right). \tag{57}$$

The structure of matrix elements of other local operators that are mutually local with the Fermi field is analogous: Only a very small fraction of all off-diagonal matrix elements are nonzero.

B. Local operators that are not local relative to the Fermi field

As an example of a local operator that is not local relative to the Fermi field, we consider the Bose field operator, which fulfills

$$\Phi(x)\Psi(y) = \text{sgn}(x - y)\Psi(y)\Phi(x). \tag{58}$$

A convenient representation for the matrix elements of the Bose field operator at positive values of c was derived in Ref. [33]. In the impenetrable limit, the matrix element between a state $|\boldsymbol{\lambda}\rangle$ with N particles and a state $|\boldsymbol{\mu}\rangle$ is nonvanishing only if the latter has $N - 1$ particles; it then reads

$$\frac{|\langle \boldsymbol{\mu}|\Phi(0)|\boldsymbol{\lambda}\rangle|^2}{\langle \boldsymbol{\lambda}|\boldsymbol{\lambda}\rangle\langle \boldsymbol{\mu}|\boldsymbol{\mu}\rangle} = \frac{2^{2N-2}}{L^{2N-1}}\prod_{j=1}^{N}\prod_{k=1}^{N-1}\frac{1}{(\lambda_j - \mu_k)^2} \times \prod_{j>k}^{N}(\lambda_j - \lambda_k)^2\prod_{j>k}^{N-1}(\mu_j - \mu_k)^2. \tag{59}$$

This result already shows that all matrix elements compatible with the simple particle-number selection rule—that $\Phi(0)$ changes particle number by one—are nonvanishing. This finding is in marked contrast to what we have for spatially local operators that are local relative to the Fermi field.

1. Matrix elements involving different macrostates

If $|\lambda\rangle$ and $|\mu\rangle$ belong to different macrostates, say, with root densities $\rho_0(\lambda)$ and $\rho_1(\mu)$, respectively, it is straightforward to determine the leading contribution (in L) for large system sizes by noting that

$$\frac{1}{L^2}\ln\left[\frac{|\langle\mu|\Phi(0)|\lambda\rangle|^2}{\langle\lambda|\lambda\rangle\langle\mu|\mu\rangle}\right] = -\frac{1}{L^2}\sum_{j,k}\ln(\lambda_j-\mu_k)^2 + \frac{1}{L^2}\sum_{j>k}^{N}\ln(\lambda_j-\lambda_k)^2 + \frac{1}{L^2}\sum_{j>k}^{N-1}\ln(\mu_j-\mu_k)^2 + o(L^0). \tag{60}$$

Turning sums into integrals, we obtain

$$\frac{1}{L^2}\ln\left[\frac{|\langle\mu|\Phi(0)|\lambda\rangle|^2}{\langle\lambda|\lambda\rangle\langle\mu|\mu\rangle}\right] = \frac{1}{2}\int_{-\infty}^{\infty} d\lambda d\mu[\rho_0(\lambda)-\rho_1(\lambda)][\rho_0(\mu)-\rho_1(\mu)]\ln(\lambda-\mu)^2 + o(L^0). \tag{61}$$

Thus, we see that the matrix elements involving two different macrostates are extremely small,

$$\frac{|\langle\mu|\Phi(0)|\lambda\rangle|^2}{\langle\lambda|\lambda\rangle\langle\mu|\mu\rangle} \propto e^{-c_{\rho_0,\rho_1}L^2}. \tag{62}$$

This behavior is in stark contrast to the behavior of off-diagonal matrix elements in different macrostates in nonintegrable models as predicted by the ETH. We note that the subleading terms (in system size) in Eq. (60) depend on the details of the microstates $|\mu\rangle$ and $|\lambda\rangle$ and not only on the macrostate information encoded in $\rho_{0,1}(\lambda)$.

2. Typical matrix elements in the same thermal macrostate

When $|\lambda\rangle$ and $|\mu\rangle$ belong to the same macrostate, the leading (in L) term [Eq. (62)] vanishes, as can be seen by taking $\rho_1(\lambda) = \rho_0(\lambda)$.

In order to understand the structure of the subleading terms, we first fix $|\lambda\rangle$ to correspond to a thermal state at temperature $T = 10$ and density $D = 1$ and then numerically determine the probability distribution of

$$\mathfrak{M}_{\lambda,\mu} = -\frac{1}{L}\ln\left[\frac{|\langle\mu|\Phi(0)|\lambda\rangle|^2}{\langle\lambda|\lambda\rangle\langle\mu|\mu\rangle}\right], \tag{63}$$

where $|\mu\rangle$ are microstates corresponding to the same thermal macrostate and are taken to have energy eigenvalues such that $|E(\mu) - E(\lambda)| < 25$. When $|\lambda\rangle$ has L rapidities, the states $|\mu\rangle$ must have $L-1$ particles in order for $\mathfrak{M}_{\lambda,\mu}$ to be nonvanishing.

In Fig. 4, we plot the probability distributions, obtained by sampling $\langle\mu|$, for three different choices of the microstate $|\lambda\rangle$. Here, all states belong to the same thermal macrostate with temperature $T = 10$ and $L = N = 512$. We see that the probability distributions are very sensitive to the details of the microstate $|\lambda\rangle$ and not only macrostate information encoded in $\rho_0(\lambda)$. The smallest mean value of $\mathfrak{M}_{\lambda,\mu}$ (corresponding to the largest average absolute value of the matrix elements) is obtained when $|\lambda\rangle$ corresponds to the smooth microstate, cf. the green histogram in Fig. 1. The yellow histogram in Fig. 4, corresponding to the second-smallest mean of the distribution, is obtained by choosing a microstate with the distribution of half-odd integers shown in Fig. 5. We see that the distribution of integers in Fig. 5 does not reproduce the thermodynamic root density as well as the smooth state does. This notion

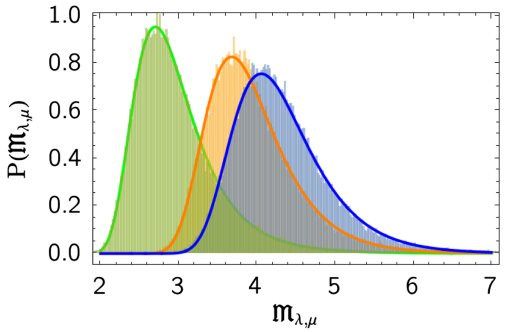

FIG. 4. Normalized histograms of $|\mathfrak{M}_{\lambda,\mu}|$ for three different microstates $|\lambda\rangle$ (see text) and 50,000 states $|\mu\rangle$ with $L = N = 512$ (respectively in yellow, blue, green, and red), where $|\lambda\rangle$ and $|\mu\rangle$ are microstates corresponding to the thermal macrostate at temperature $T = 10$. The solid lines are fits to Fréchet distribution functions.

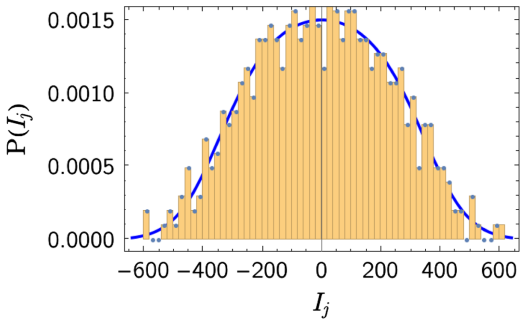

FIG. 5. Normalized histogram for the distribution of integers for $L = N = 512$ and a microstate corresponding to a thermal macrostate with $c = \infty$, $\beta = 0.1$, and $D = 1$.

can be quantified by computing the mean-squared distance between the histograms with bins $[\nu_1, \ldots, \nu_{n_{\rm bin}+1}]$ to the thermodynamic result

$$\Delta = \sum_{j=1}^{n_{\rm bin}} \left[n_j - \int_{\nu_j}^{\nu_{j+1}} d\nu \frac{2\pi}{L} \rho\left(\frac{2\pi}{L}\nu\right) \right]^2. \tag{64}$$

Here, n_j is the occupation of bin j and $\rho(x)$ the thermodynamic root density describing the macrostate under consideration. The third microstate considered in Fig. 4 (blue histogram) has the largest distance, in this sense, to the thermodynamic root density. This finding suggests that the larger the deviations of the root distribution of $|\lambda\rangle$ from the thermodynamic root density, the smaller the typical matrix elements $\mathfrak{M}_{\lambda,\mu}$ (sampled over $\langle\mu|$) become.

The solid lines in Fig. 4 are fits to Fréchet distribution functions,

$$P_{\alpha,\beta,\nu}(x) = \begin{cases} \frac{\alpha}{\beta}\left(\frac{x-\nu}{\beta}\right)^{-\alpha-1} \exp\left[-\left(\frac{x-\nu}{\beta}\right)^{-\alpha}\right] & \text{if } x > \nu \\ 0 & \text{else.} \end{cases} \tag{65}$$

We find that fits to $P_{\alpha,\beta,\nu}(x)$ provide excellent descriptions of our numerical PDFs in all the cases we have considered. The parameters α, β, ν depend not only on macrostate information but also on details of the microstate $|\lambda\rangle$, i.e.,

$$\alpha = \alpha_\lambda, \qquad \beta = \beta_\lambda, \qquad \nu = \nu_\lambda. \tag{66}$$

The next question we want to address is how the PDFs of $\mathfrak{M}_{\lambda,\mu}$ scale with system size. To address this issue, we work with the smooth state because it can be readily scaled up with system size. We observe that we can achieve excellent data collapse if we shift the matrix elements by an L-dependent constant

$$M_{\lambda,\mu} = \mathfrak{M}_{\lambda,\mu} - c_0 \ln(L). \tag{67}$$

In Fig. 6, we show the histograms of $M_{\lambda,\mu}$ when sampled over the states $\langle\mu|$ for a thermal macrostate with temperature $T = 10$ and density $D = N/L = 1$ for four different values of L and $c_0 = 0.375801$. We observe that the data for different system sizes collapse very nicely. Other microstates are more difficult to scale up in system size, but supposedly an analogous data collapse of shifted distributions occurs.

In order to remove the explicit dependence of $P(M_{\lambda,\mu})$ on the ket microstate $|\lambda\rangle$, we may sample the latter in the same energy window as the bra states $\langle\mu|$. Denoting the energy density in the thermodynamic limit by e_∞, we take this window to be $|E - Le_\infty| < 7.5$. The resulting probability distributions of appropriately shifted matrix elements (67) are shown in Fig. 7 for a range of system sizes. Fixing the constant in Eq. (67) to be $c_0 = 0.755474$ leads to an excellent data collapse, and the resulting probability distribution is again well described by a Fréchet distribution.

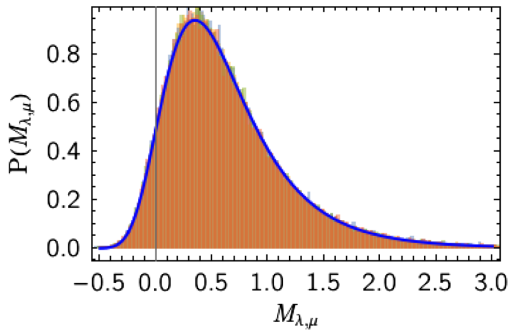

FIG. 6. Normalized histograms of $M_{\lambda,\mu}$ for the smooth microstate $|\lambda\rangle$ (see text) and 50 000 states $|\mu\rangle$ with $L = N = 128, 256, 512, 1024$ (respectively in yellow, blue, green, and red), where $|\lambda\rangle$ and $|\mu\rangle$ are microstates corresponding to the thermal macrostate at temperature $T = 10$. The solid line is a Fréchet distribution function with fitted parameters $\alpha = 12.8894$, $\beta = 5.04354$, and $\nu = -4.66742$.

3. Typical matrix elements in the same nonthermal macrostate

We have also considered typical matrix elements in atypical macrostates. As a particular example, we present results for the distribution function of integers shown in Fig. 8. These results correspond to a generalized Gibbs ensemble with momentum distribution function

$$\rho(\lambda) = \frac{1}{2\pi\left[1 + e^{(\lambda^2-\mu)/T+\mu_3\lambda^4+\mu_4\lambda^6}\right]}, \tag{68}$$

where $T = 20$, $\mu = 32.0846$, $\mu_3 = -0.01$, and $\mu_4 = 0.00015$. The densities of energy and the fourth and sixth conservation laws of the Lieb-Liniger model for this macrostate in the thermodynamic limit are, respectively,

$$e_\infty = 32.0846, \quad q^{(4)} = 1270.96, \quad q^{(6)} = 55027.1. \tag{69}$$

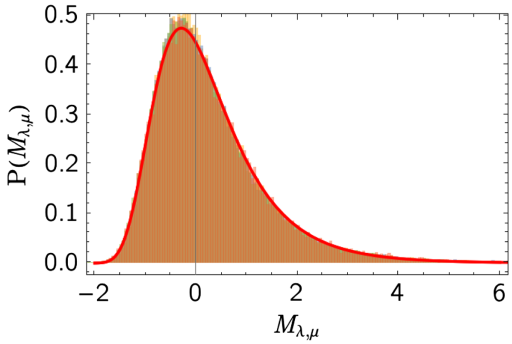

FIG. 7. Normalized histograms of $M_{\lambda,\mu}$, where both $|\lambda\rangle$ and $|\mu\rangle$ are sampled from a thermal macrostate at $T = 10$, $D = 1$ in a fixed energy window $|E - Le_\infty| < 7.5$ with $L = N = 64, 128, 256, 512$ (respectively in yellow, blue, green, and orange). The solid line is a Fréchet distribution function with fitted parameters $\alpha = 13.0393$, $\beta = 10.1444$, and $\nu = -10.3779$.

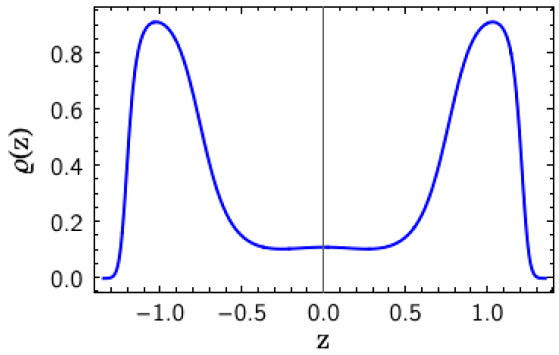

FIG. 8. Distribution function of I_j/L for a nonthermal macrostate.

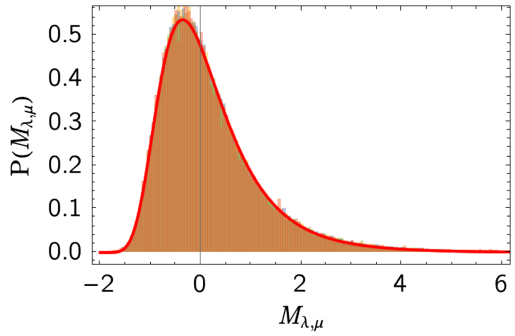

FIG. 9. Normalized histograms of $M_{\lambda,\mu}$, where both $|\lambda\rangle$ and $|\mu\rangle$ are sampled from the atypical macrostate described by the root density (68) in fixed windows of the energy and relevant higher conservation laws (see text) with $L = N = 64$, 128, 192, 256 (respectively in yellow, blue, green, and orange). The solid line is a Fréchet distribution function with fitted parameters $\alpha = 8.99436$, $\beta = 6.22114$, and $\nu = -6.50698$.

In order to sample the macrostate, we have chosen windows for the eigenvalues $|E - Le_\infty| < 20$, $|\nu^{(4)} - Lq^{(4)}| < 800$, and $|\nu^{(6)} - Lq^{(6)}| < 34300$. We note that if we do not restrict the eigenvalues, the probability distribution shifts by a small amount. The PDF of $M_{\lambda,\mu}$, where both $|\lambda\rangle$ and $|\mu\rangle$ are sampled from the atypical macrostate constructed in this way and the constant shift is taken to be $c_0 = 0.680685$, is shown for a range of system sizes $64 \le N \le 256$ in Fig. 9. We observe an excellent data collapse to a PDF that is well described by a Fréchet distribution function with fitted parameters $\alpha = 8.99436$, $\beta = 6.22114$, and $\nu = -6.50698$.

Our results in this subsection can be summarized as follows.

(i) If we fix the ket state $|\lambda\rangle$, then typical off-diagonal matrix elements in the same macrostate scale with system size as

$$\frac{|\langle\mu|\Phi(0)|\lambda\rangle|^2}{\langle\lambda|\lambda\rangle\langle\mu|\mu\rangle} \propto e^{-c_0 L\ln(L)-c_1 L}. \tag{70}$$

The corresponding probability distribution depends on details of $|\lambda\rangle$, i.e., the multivariate distribution function on (half-odd) integers and not only on macrostate information. In particular, the two constants $c_{0,1}$ depend on the choice of $|\lambda\rangle$.

(ii) The probability distribution is well fitted by a Fréchet distribution, where the parameters depend on the choice of $|\lambda\rangle$.

(iii) If we sample both the bra and ket states over the same energy window, typical matrix elements again scale with system size as Eq. (70), and the resulting probability distribution is again well fitted by a Fréchet distribution. In this case, we expect c_0 to depend only on macrostate information.

An immediate consequence of the $e^{-c_0 L\ln(L)}$ factor in Eq. (70) is that typical matrix elements will not contribute to correlation functions of local operators in the thermodynamic limit. To see this consequence, let us consider a two-point function in an energy eigenstate (generalized microcanonical ensemble, cf. Ref. [64]) corresponding to a macrostate characterized by the density $\varrho_0(z)$,

$$F(x,t) = \langle\lambda|\Phi^\dagger(x,t)\Phi(0,0)|\lambda\rangle. \tag{71}$$

Employing a Lehmann representation and using the fact that matrix elements involving eigenstates corresponding to different macrostates ϱ_1 scale as $e^{-c_{\varrho_0,\varrho_1}L^2}$, we have

$$F(x,t) = \sum_\mu |\langle\lambda|\Phi^\dagger(0,0)|\mu\rangle|^2 e^{-it(E_\mu - E_\lambda)+ix(P_\mu - P_\lambda)} + o(L^0), \tag{72}$$

where the sum is over all solutions to the Bethe ansatz equations that correspond to the macrostate characterized by $\varrho_0(z)$. Typical matrix elements cannot contribute to this sum because they scale with system size like Eq. (70), while their number scales as $e^{Ls_{\varrho_0}}$, where s_{ϱ_0} is the thermodynamic entropy density of the macrostate under consideration. The spectral sum (72) must therefore be determined by "anomalously large" matrix elements in the "nose" of the probability distribution function. We now turn to the question of how to characterize them.

4. Rare large matrix elements in the same macrostate

Which states $\langle\mu|$ give anomalously large matrix elements $|\langle\mu|\Phi(0,0)|\lambda\rangle|$ for a given ket state $|\lambda\rangle$? A natural guess is that each of the rapidities μ_j should be very close to one the rapidities λ_k of the state $|\lambda\rangle$, so that the factor $(\lambda_k - \mu_j)^{-2}$ in the expression of the matrix element (59) becomes very large. This intuition is indeed correct, as was shown for the case of the transverse-field Ising model in Ref. [65] (see also Refs. [66–68]). In Fig. 10, we present histograms of matrix elements (63) for a smooth thermal state $|\lambda\rangle$

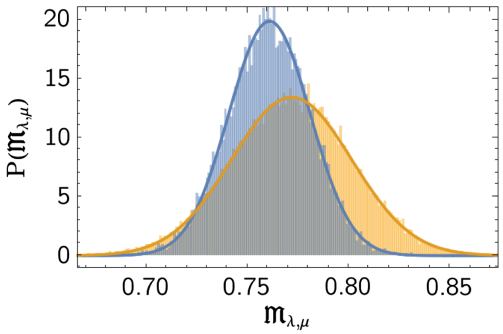

FIG. 10. Normalized histograms of the matrix elements of the field operator between a smooth thermal state with $D = 1$ and $\beta = 0.1$ and the atypical states in the set $\mathfrak{S}_0$ described in the text for $L = 128$ (yellow) and $L = 256$ (blue). The solid lines are fits to normal distributions.

at density $D = 1$ and inverse temperature $\beta = 0.1$, and a class of states $\langle\boldsymbol{\mu}|$ selected as follows:

(i) We randomly remove one of the rapidities in $\{\lambda_1, \ldots, \lambda_N\}$.

(ii) In the remaining set, we randomly shift each λ_j by $\pm\pi/L$ under the constraint that all rapidities in the resulting set $\{\mu_1, \ldots, \mu_{N-1}\}$ must be different. In this way, each μ_n is "paired" with one of the λ_j in the sense that their difference is as small as possible.

The set $\mathfrak{S}_0(\boldsymbol{\lambda})$ of states $\langle\boldsymbol{\mu}|$ constructed in this way is clearly exponentially large in system size. We may characterize $\mathfrak{S}_0(\boldsymbol{\lambda})$ in terms of a distance ($\lambda_j = 2\pi I_j/L$, $\mu_k = 2\pi J_k/L$),

$$d(\boldsymbol{\lambda},\boldsymbol{\mu}) \equiv \min_{P\in S_N} \sum_{j=1}^{N-1} (J_j - I_{P_j})^2, \tag{73}$$

as the set of all eigenstates such that

$$d(\boldsymbol{\lambda},\boldsymbol{\mu}) = \frac{N-1}{4}. \tag{74}$$

We observe that the matrix elements for this class of states are indeed much larger than for typical thermal states, cf. Fig. 4. As the system size is increased, the probability distribution narrows and shifts towards smaller values (i.e., large matrix elements). We find that $P(\mathfrak{M}_{\lambda,\boldsymbol{\mu}})$ is well described by a normal distribution.

While the matrix elements constructed in this way are large, their contribution to local correlation functions vanishes in the thermodynamic limit. This finding is most easily seen by considering the low-density regime. Here, the distance between neighboring integers in a thermal state is typically much larger than 1, which makes it easy to count states.

(1) The number of states in $\mathfrak{S}_0(\boldsymbol{\lambda})$ is $N2^{N-1}$ in the low-density limit. The magnitude of the corresponding matrix elements with the smooth thermal state can be estimated as

$$\mathfrak{M}_{\lambda,\boldsymbol{\mu}} \approx -D\ln\left[\frac{4}{\pi^2}\right] + \frac{\ln(L)}{L} - \frac{2\ln(\pi/2)}{L}. \tag{75}$$

Hence,

$$\frac{|\langle\boldsymbol{\mu}|\Phi(0)|\boldsymbol{\lambda}\rangle|^2}{\langle\boldsymbol{\lambda}|\boldsymbol{\lambda}\rangle\langle\boldsymbol{\mu}|\boldsymbol{\mu}\rangle} \propto e^{LD\ln[\frac{4}{\pi^2}]}, \tag{76}$$

while the number of states in $\mathfrak{S}_0(\boldsymbol{\lambda})$ scales exponentially with system size,

$$|\mathfrak{S}_0(\boldsymbol{\lambda})| \propto e^{DL\ln(2)}. \tag{77}$$

Concomitantly, the contribution of such states to two-point functions vanishes in the thermodynamic limit as $e^{LD\ln(8/\pi^2)}$.

(2) We next consider the set of states $\mathfrak{S}_1$ that differs from $\mathfrak{S}_0$ by adding a single "soft mode," by which we refer to one of the J_j differing from its corresponding I_k by $\pm(m+\frac{1}{2})$ rather than $\pm\frac{1}{2}$ [where we keep $m = \mathcal{O}(L^0)$]. States in $\mathfrak{S}_1$ have

$$d(\boldsymbol{\lambda},\boldsymbol{\mu}) = \frac{N-1}{4} + \frac{(2m+1)^2-1}{4}. \tag{78}$$

The same kind of argument as before now gives

$$\mathfrak{M}_{\lambda,\boldsymbol{\mu}} \sim -D\ln\left[\frac{4}{\pi^2}\right] + \frac{\ln(L)}{L} + \frac{2\ln\left(\frac{2(2m+1)}{\pi}\right)}{L} \tag{79}$$

while the number of states increases to

$$N(N-1)2^{N-1}. \tag{80}$$

This result shows that the contribution of such states to two-point functions again vanishes in the thermodynamic limit.

(3) The above considerations generalize to a finite number of soft modes. The rare states of interest therefore involve an extensive number of soft modes, cf. Refs. [65–68]. It was shown in Ref. [46] how to sum over soft modes in an arbitrary macrostate at low particle density and obtain an explicit expression for the single-boson Green's function.

VII. MATRIX ELEMENTS IN INTERACTING THEORIES

The matrix elements of local operators between two normalized Bethe states have been derived in Refs. [31–34]. In the case of the density operator, the

square of the matrix element between two normalized eigenstates $|\boldsymbol{\lambda}\rangle, |\boldsymbol{\mu}\rangle$ with respective numbers of Bethe roots N, N' reads

$$\frac{|\langle\boldsymbol{\lambda}|\hat{\rho}(0)|\boldsymbol{\mu}\rangle|^2}{\langle\boldsymbol{\lambda}|\boldsymbol{\lambda}\rangle\langle\boldsymbol{\mu}|\boldsymbol{\mu}\rangle} = \delta_{N,N'}\frac{(\sum_{i=1}^N \mu_i-\lambda_i)^2}{L^{2N}\mathcal{N}_{\boldsymbol{\lambda}}\mathcal{N}_{\boldsymbol{\mu}}}\frac{\prod_{i\neq j}(\lambda_i-\lambda_j)(\mu_i-\mu_j)}{\prod_{i,j}(\lambda_i-\mu_j)^2}\prod_{i\neq j}\frac{\lambda_i-\lambda_j+ic}{\mu_i-\mu_j+ic} \times\left|\det_{i,j\neq p}\left[(V_i^+-V_i^-)\delta_{ij}+i(\mu_i-\lambda_i)\prod_{k\neq i}\frac{\mu_k-\lambda_i}{\lambda_k-\lambda_i}\left(\frac{2c}{(\lambda_i-\lambda_j)^2+c^2}-\frac{2c}{(\lambda_p-\lambda_j)^2+c^2}\right)\right]\right|^2. \tag{81}$$

Here, $p\in\{1,\ldots,N\}$ can be freely chosen,

$$V_i^{\pm}=\prod_{k=1}^N\frac{\mu_k-\lambda_i\pm ic}{\lambda_k-\lambda_i\pm ic}, \tag{82}$$

and $\mathcal{N}_{\boldsymbol{\lambda}}$ is given by

$$\mathcal{N}_{\boldsymbol{\lambda}}=\det\left[\delta_{ij}\left(1+\frac{1}{L}\sum_{k=1}^N\frac{2c}{c^2+\lambda_{i,k}^2}\right)-\frac{1}{L}\frac{2c}{c^2+\lambda_{i,j}^2}\right]. \tag{83}$$

When presenting results for the statistics of such matrix elements, we consider logarithmic expressions like

$$\mathfrak{M}_{\boldsymbol{\lambda},\boldsymbol{\mu}}^{\rho}=-\frac{1}{L}\ln\left[\frac{|\langle\boldsymbol{\lambda}|\rho(0)|\boldsymbol{\lambda}\rangle|^2}{\langle\boldsymbol{\lambda}|\boldsymbol{\lambda}\rangle\langle\boldsymbol{\mu}|\boldsymbol{\mu}\rangle}\right]. \tag{84}$$

In the following, we also use the explicit expressions for the matrix elements of g_2 given in Ref. [34]. In the case $P_{\boldsymbol{\lambda}}\neq P_{\boldsymbol{\mu}}$, the following relation holds:

$$\frac{|\langle\boldsymbol{\lambda}|g_2(0)|\boldsymbol{\mu}\rangle|^2}{\langle\boldsymbol{\lambda}|\boldsymbol{\lambda}\rangle\langle\boldsymbol{\mu}|\boldsymbol{\mu}\rangle}=\frac{|\langle\boldsymbol{\lambda}|\hat{\rho}(0)|\boldsymbol{\mu}\rangle|^2}{\langle\boldsymbol{\lambda}|\boldsymbol{\lambda}\rangle\langle\boldsymbol{\mu}|\boldsymbol{\mu}\rangle}\left(\frac{\mathcal{J}_{\boldsymbol{\lambda},\boldsymbol{\mu}}}{6c(P_{\boldsymbol{\lambda}}-P_{\boldsymbol{\mu}})^2}\right)^2, \tag{85}$$

where

$$\mathcal{J}_{\boldsymbol{\lambda},\boldsymbol{\mu}}=(P_{\boldsymbol{\lambda}}-P_{\boldsymbol{\mu}})^4-4(P_{\boldsymbol{\lambda}}-P_{\boldsymbol{\mu}})\left(\nu_{\boldsymbol{\lambda}}^{(3)}-\nu_{\boldsymbol{\mu}}^{(3)}\right)+3(E_{\boldsymbol{\lambda}}-E_{\boldsymbol{\mu}})^2. \tag{86}$$

The relation (85) has important consequences because, by construction, we have

$$P_{\boldsymbol{\lambda}},E_{\boldsymbol{\lambda}},\nu_{\boldsymbol{\lambda}}^{(3)}\sim L. \tag{87}$$

This result allows us to conclude that

$$\mathfrak{M}_{\boldsymbol{\lambda},\boldsymbol{\mu}}^{g_2}=\mathfrak{M}_{\boldsymbol{\lambda},\boldsymbol{\mu}}^{\rho}+\mathcal{O}\left(\frac{\ln(L)}{L}\right), \tag{88}$$

which means that, up to finite-size corrections, the statistical properties of $\mathfrak{M}_{\boldsymbol{\lambda},\boldsymbol{\mu}}^{g_2}$ and $\mathfrak{M}_{\boldsymbol{\lambda},\boldsymbol{\mu}}^{\rho}$ should be identical. We verify this by explicit numerical computations below.

A. Diagonal matrix elements in interacting theories

In order to determine the statistical properties of diagonal matrix elements for $c<\infty$, we focus on the interaction potential $g_2(x)$ [Eq. (46)] because diagonal matrix elements of the density operator $\rho(x)$ are trivial due to particle-number conservation. We further restrict our analysis to thermal macrostates. We determine the probability distribution of

$$\mathfrak{g}_2(\boldsymbol{\mu})=\frac{\langle\boldsymbol{\mu}|g_2(0)|\boldsymbol{\mu}\rangle}{\langle\boldsymbol{\mu}|\boldsymbol{\mu}\rangle}, \tag{89}$$

where $|\boldsymbol{\mu}\rangle$ are thermal microstates with energy $E_{\boldsymbol{\mu}}$, which we sample in an energy window $\omega=E_{\boldsymbol{\mu}}-E_{\text{smooth}}\in[-50,50]$. Here, E_{smooth} is the energy of the smooth thermal microstate at a given temperature and system size. In Fig. 11, we show the resulting probability distribution for $T=10$, $L=512$, and $c=4$. As we increase the system size, the average of the PDF converges, as expected, to the thermodynamic limit result. What is of interest is the scaling of the standard deviation of the PDF with system size. This scaling is shown for three different values of c and thermal microstates at temperature $T=10$ and density $D=1$ in Fig. 12 for system sizes $L=64$, 128, 256, 512. We see that the standard deviation collapses to zero. Motivated by the results in the $c=\infty$ limit, we have fitted the data to second-order polynomials in $x=L^{-\frac{1}{2}}$,

$$f(x)=a_1x+a_2x^2. \tag{90}$$

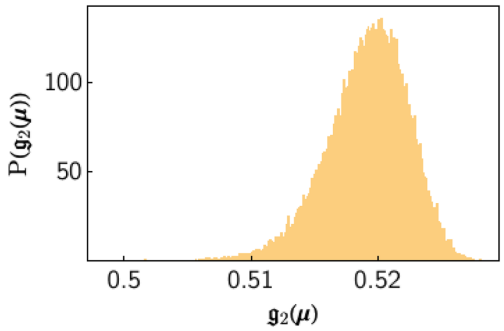

FIG. 11. Probability distribution of $\mathfrak{g}_2(\boldsymbol{\mu})$ for thermal microstates at $T=10$, $L=512$, and $c=4$, where we sample in an energy window as described in the main text.

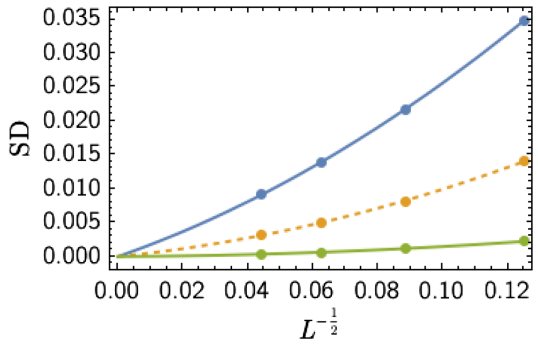

FIG. 12. Standard deviations of $P(\mathfrak{g}_2(\boldsymbol{\mu}))$ for thermal microstates at $T = 10$, $D = 1$, and at $c = 1$ (blue), $c = 4$ (yellow), and $c = 16$ (green). The lines are fits as described in the main text.

The good quality of the fits suggests that, for large system sizes, the standard deviation scales as $L^{-1/2}$, as was previously observed for nonthermal states in the spin-1/2 XXZ chain [19,69]. The situation is very different in nonintegrable models, where the scaling of the standard deviation is exponential in system size [7–9].

B. Off-diagonal matrix elements in interacting theories

We now turn to our main topic of interest, off-diagonal matrix elements in interacting theories. We start by considering matrix elements of local operators between two different macrostates. On physical grounds, these matrix elements are expected to be very small, and our aim is to ascertain their scaling with system size at a fixed density.

1. Off-diagonal matrix elements between two different thermal macrostates

Motivated by our results for matrix elements between two different macrostates in the noninteracting case, we examine the probability distributions of

$$\frac{1}{L}\mathfrak{M}^{\mathcal{O}}_{\boldsymbol{\lambda},\boldsymbol{\mu}} = \frac{1}{L^2}\ln\left(\frac{|\langle\boldsymbol{\mu}|\mathcal{O}(0)|\boldsymbol{\lambda}\rangle|^2}{\langle\boldsymbol{\lambda}|\boldsymbol{\lambda}\rangle\langle\boldsymbol{\mu}|\boldsymbol{\mu}\rangle}\right), \qquad \mathcal{O} = \hat{\rho},\ g_2. \tag{91}$$

In particular, we focus on the medians $m_{\mathcal{O}}$ and standard deviations $s_{\mathcal{O}}$ of the respective PDFs as functions of particle number N, which, for simplicity, is taken to be equal to L throughout. We generate random samples of 1000 microstates $\langle\boldsymbol{\mu}|$ and $|\boldsymbol{\lambda}\rangle$ that belong to thermal macrostates at two different temperatures T_1 and T_2, and we use them to numerically compute 20 000 matrix elements. Some results from this analysis are shown in Figs. 13 (for g_2) and 14 (for $\hat{\rho}$).

We observe the following:

(i) The standard deviations of the PDFs narrow with increasing L.

(ii) The medians m_{g_2} and m_ρ approach finite limiting values for large system sizes that depend on the macrostates but appear to be independent of which local operator, $g_2(0)$ or $\hat{\rho}(0)$, we consider. Numerical extrapolations in L^{-1} give limiting values that are close to the values we obtained for the Bose field in the impenetrable case,

$$\frac{1}{L}\mathfrak{M}^{\mathcal{O}}_{\boldsymbol{\lambda},\boldsymbol{\mu}} \approx \frac{1}{2}\int_{-\infty}^{\infty} d\lambda d\mu [\rho_0(\lambda)-\rho_1(\lambda)][\rho_0(\mu)-\rho_1(\mu)] \times \ln(\lambda-\mu)^2 + o(L^0). \tag{92}$$

Here, $\rho_0(\lambda)$ and $\rho_1(\lambda)$ are the root densities of the two macrostates under consideration. The fact that the extrapolated values for m_{g_2} and m_ρ are the same is easy to understand from the explicit relation (85) between their matrix elements, which implies that, for $P_\lambda \neq P_\mu$,

$$\frac{1}{L}[\mathfrak{M}^{g_2}_{\boldsymbol{\lambda},\boldsymbol{\mu}} - \mathfrak{M}^{\hat{\rho}}_{\boldsymbol{\lambda},\boldsymbol{\mu}}] = \frac{1}{L^2}\ln\left[\frac{\mathcal{J}^2_{\boldsymbol{\lambda},\boldsymbol{\mu}}}{6c(P_\lambda - P_\mu)^2}\right]^2. \tag{93}$$

The right-hand side scales with system size as $\ln(L)/L^2$ and hence vanishes in the thermodynamic limit.

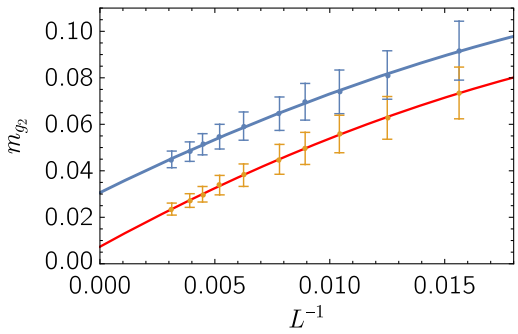

FIG. 13. Medians (dots) m_{g_2} and standard deviations s_{g_2} (error bars) of the PDFs of $M^{g_2}_{\boldsymbol{\lambda},\boldsymbol{\mu}}/L$, where $|\boldsymbol{\lambda}\rangle$ and $|\boldsymbol{\mu}\rangle$ are sampled, respectively, from thermal macrostates at $T_1 = 10$, $T_2 = 5$ (blue symbols) and $T_1 = 10$, $T_2 = 7.5$ (red symbols) for $D = 1$ in a fixed energy window $|E - Le_\infty| < 25$. The solid lines are polynomial fits.

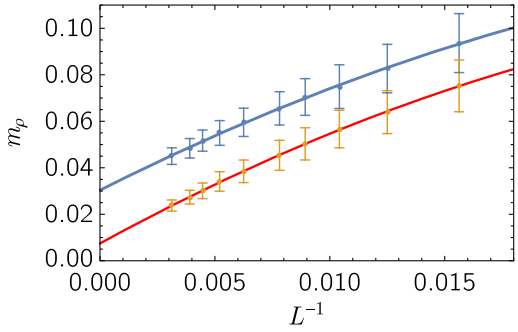

FIG. 14. Same as Fig. 13 for matrix elements of the density operator $\hat{\rho}$.

The results of this section are summarized in the following conjecture: Matrix elements involving microstates belonging to two different macrostates scale with system size as

$$\frac{|\langle \boldsymbol{\mu}|\mathcal{O}(0)|\boldsymbol{\lambda}\rangle|^2}{\langle \boldsymbol{\lambda}|\boldsymbol{\lambda}\rangle\langle \boldsymbol{\mu}|\boldsymbol{\mu}\rangle} \propto e^{-c^{\mathcal{O}}_{\rho_0,\rho_1} L^2}. \tag{94}$$

Here, $c^{\mathcal{O}}_{\rho_0,\rho_1}$ is a constant that depends on the macrostates under consideration and *a priori* on the operator $\mathcal{O}$. The numerical results presented above are consistent with $c^{\mathcal{O}}_{\rho_0,\rho_1}$ being independent of $\mathcal{O}$ and given by minus the right-hand side of Eq. (92). This behavior is in stark contrast to the behavior of off-diagonal matrix elements in different macrostate nonintegrable models as predicted by the ETH.

2. *Off-diagonal matrix elements between microstates belonging to the same thermal macrostates*

We now turn to matrix elements involving microstates that belong to the same macrostate. The question we want to address is how the corresponding PDFs scale with system size. In order to remove the sensitive dependence on the ket microstate, we sample the ket states $|\boldsymbol{\lambda}\rangle$ over the same energy window as the bra state $\langle \boldsymbol{\mu}|$. Denoting the energy density in the thermodynamic limit by e_∞, we take this window to be $|E - Le_\infty| < 25$ in the figures shown below. For simplicity, we focus on thermal macrostates. We observe that we can achieve excellent data collapse for the PDFs for different system sizes if we shift the matrix elements by an L-dependent constant

$$M^{\mathcal{O}}_{\boldsymbol{\lambda},\boldsymbol{\mu}} = \mathfrak{M}^{\mathcal{O}}_{\boldsymbol{\lambda},\boldsymbol{\mu}} - c^{\mathcal{O}}_0 \ln(L), \qquad \mathcal{O} = \hat{\rho}, g_2. \tag{95}$$

The resulting probability distributions of appropriately shifted matrix elements (95) of the interaction operator $g_2(0)$ in a thermal macrostate at $T = 5$, $D = 1$ are shown in Fig. 15 for $L = N = 64, 96, 160, 224$. Here, we have fixed the constant in Eq. (95) to be $c^{g_2}_0 = 0.754585$, which leads to a very good data collapse. The resulting probability distribution is well described by a Fréchet distribution with fitted parameters $\alpha = 16.1378$, $\beta = 14.2188$, and $\nu = -14.2223$.

The choice $c^{\rho}_0 = c^{g_2}_0$ leads to a good data collapse, as shown in Fig. 16, and the resulting PDF is well described by a Fréchet distribution with fitted parameters $\alpha = 17.3467$, $\beta = 15.536$, and $\nu = -15.5163$. The fact that the fitted Fréchet distributions differ slightly for $\hat{\rho}$ and g_2 is a result of the finite-size effects that scale as $\ln(L)/L$, cf. the discussion surrounding Eq. (88).

In Fig. 17, we show the probability distributions of appropriately shifted matrix elements [Eq. (95)] of the interaction operator $g_2(0)$ in a thermal macrostate at $T = 10$, $D = 1$ for $L = N = 64, 96, 128, 192, 224$. Our choice of shift parameter $c^{g_2} = -0.995755$ is again seen to

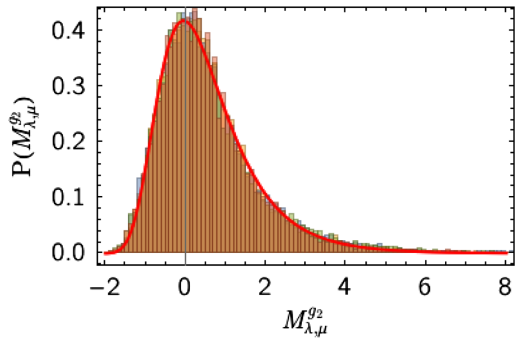

FIG. 15. Normalized histograms of $M^{g_2}_{\lambda,\mu}$, where both $|\lambda\rangle$ and $|\mu\rangle$ are sampled from a thermal macrostate at $T = 5$, $D = 1$ in a fixed energy window $|E - Le_\infty| < 25$, with $L = N = 64$, 96, 160, 224 (respectively in yellow, blue, green, and orange). The solid line is a Fréchet distribution function with fitted parameters $\alpha = 16.1378$, $\beta = 14.2188$, and $\nu = -14.2223$.

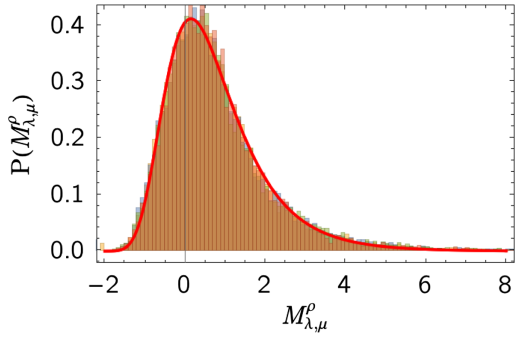

FIG. 16. Normalized histograms of $M^{\rho}_{\lambda,\mu}$, where both $|\lambda\rangle$ and $|\mu\rangle$ are sampled from a thermal macrostate at $T = 5$, $D = 1$ in a fixed energy window $|E - Le_\infty| < 25$, with $L = N = 64$, 96, 160, 224 (respectively in yellow, blue, green, and orange).The solid line is a Fréchet distribution function with fitted parameters $\alpha = 17.3467$, $\beta = 15.536$, and $\nu = -15.5163$.

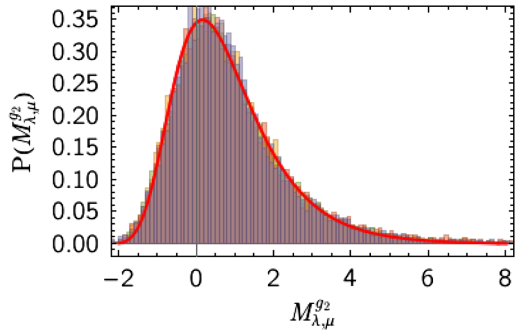

FIG. 17. Normalized histograms of $M^{g_2}_{\lambda,\mu}$, where both $|\lambda\rangle$ and $|\mu\rangle$ are sampled from a thermal macrostate at $T = 10$, $D = 1$ in a fixed energy window $|E - Le_\infty| < 25$, with $L = N = 64$, 96, 128, 192, 224 (respectively in yellow, blue, green, orange, and purple). The solid line is a Fréchet distribution function with fitted parameters $\alpha = 25.9405$, $\beta = 27.2261$, and $\nu = -27.0405$.

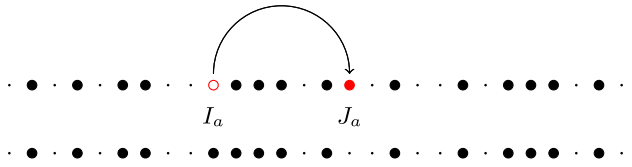

FIG. 18. Top: Bethe state that corresponds to a single-particle-hole excitation over the microstate with half-odd integers (shown at the bottom).

give a good data collapse for the histograms corresponding to different system sizes and to be well described by a fitted Fréchet distribution.

The results of this subsection are summarized in the following conjecture: Matrix elements involving microstates belonging to the same macrostate scale with system size as

$$\frac{|\langle \boldsymbol{\mu}|\mathcal{O}(0)|\boldsymbol{\lambda}\rangle|^2}{\langle \boldsymbol{\lambda}|\boldsymbol{\lambda}\rangle\langle \boldsymbol{\mu}|\boldsymbol{\mu}\rangle} \propto e^{-c_0^{\mathcal{O}} L\ln(L)-LM^{\mathcal{O}}_{\boldsymbol{\lambda},\boldsymbol{\mu}}}, \tag{96}$$

where $c_0^{\mathcal{O}}$ depends on the macrostates under consideration as well as (*a priori*) on the operator $\mathcal{O}$. The PDF for $M^{\mathcal{O}}_{\boldsymbol{\lambda},\boldsymbol{\mu}}$, where we sample both $\boldsymbol{\lambda}$ and $\boldsymbol{\mu}$, is well described by a Fréchet distribution.

C. Atypically large matrix elements

As we have seen in the previous section, typical matrix elements of local operators scale with system size as Eq. (94) or (96). Even though there are exponentially many typical states, they cannot contribute to the Lehmann representation of two-point functions, for the same reasons as discussed below Eq. (72). Hence, the matrix elements that matter in spectral representations must be in the "nose" of the PDF and concomitantly be atypically large and scale exponentially in system size. These matrix elements involve Bethe states that differ by a finite number of "particle-hole" excitations of their associated (half-odd) integers. The example of a single-particle-hole excitation is shown in Fig. 18. Given an eigenstate characterized by the set $\{I_j\}$ (shown as solid circles at the bottom), we construct an eigenstate characterized by $\{J_j\}$, obtained by changing a single half-odd integer I_a (red empty circle) to J_a (red solid circle). Carrying out a finite number of particle-hole excitations leads to matrix elements that are atypically large. The PDF of matrix elements involving a single-particle-hole excitation can be determined analytically in the large-c limit, as we show next.

1. Matrix elements of one-particle-hole states from a $1/c$ expansion

In Refs. [45,55], it was shown how to carry out a $1/c$ expansion of one-particle-hole and two-particle-hole matrix elements. In order to address statistical properties of matrix elements, we require higher orders in this expansion. In the following, we carry out such an analysis for the one-particle-hole matrix element of the density operator. Interestingly, we find a novel "infrared singularity." We show that these contributions can be exponentiated, which in turn allows us to obtain an explicit expression for the probability distribution of (the logarithm of) matrix elements in the thermodynamic limit.

Let $\boldsymbol{\lambda}$ and $\boldsymbol{\mu}$ be solutions to the Bethe ansatz equations with corresponding sets of (distinct) integers $\{I_j\}$ and $\{J_j\}$, respectively, where

$$J_j = I_j, \qquad j \neq a, \qquad J_a = I_a + n. \tag{97}$$

These solutions correspond to a hole with integer I_a (rapidity λ_a) and a particle with integer $I_a + n$ (rapidity μ_a), see Fig. 19.

The momentum difference between the two states is

$$P = \frac{2\pi n}{L}. \tag{98}$$

In the large-c limit, the following expression for the one-particle-hole matrix element of the density operator was derived in Ref. [55],

$$\left.\frac{|\langle \boldsymbol{\lambda}|\hat{\rho}(0)|\boldsymbol{\mu}\rangle|^2}{\langle \boldsymbol{\lambda}|\boldsymbol{\lambda}\rangle\langle \boldsymbol{\mu}|\boldsymbol{\mu}\rangle}\right|_{1\text{ph}} = \frac{\alpha^2}{(1+\frac{2}{cL})^2}\frac{1}{L^2}\left[1+\frac{4P'}{cL}\sum_{i\neq a}\left(\frac{1}{\lambda_{i,a}-P'}-\frac{1}{\lambda_{i,a}}\right)+\frac{4P^2}{c^2L^2}\left(-\frac{L^2}{12}\sum_{i\neq a}1+\sum_{\substack{i\neq j\\ j\neq a}}\frac{1}{\lambda_{i,j}^2}\right.\right.$$
$$\left.\left.+2\left(\sum_{i\neq a}\frac{1}{\lambda_{i,a}-P'}-\frac{1}{\lambda_{i,a}}\right)^2+\sum_{i\neq a}\frac{1}{(\lambda_{i,a}-P')^2}\right)\right]+\mathcal{O}(c^{-3}). \tag{99}$$

Here, we have defined

$$\lambda_{i,j} = \lambda_i - \lambda_j, \qquad \alpha = 1+\frac{2D}{c}, \qquad P' = \frac{P}{\alpha}. \tag{100}$$

The leading term is $1/L^2$, but at $\mathcal{O}(c^{-2})$, there is in fact an infrared divergence

$$-\frac{DP^2}{3c^2L}+\frac{4P^2}{c^2L}\left[\frac{1}{L^3}\sum_{\substack{i\neq j\\ i,j\neq a}}\frac{1}{\lambda_{i,j}^2}\right]. \tag{101}$$

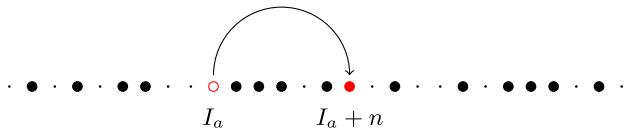

FIG. 19. Set of (half-odd) integers J_j (solid circles) corresponding to a single-particle-hole excitation over a given microstate characterized by $\{I_j\}$. One (half-odd) integer is changed from I_a (red empty circle) to I_a+n (red solid circle).

This contribution scales as L^{-1} whereas the leading term in the $1/c$ expansion scales as L^{-2}. This finding suggests the following form for the matrix elements:

$$\left.\frac{|\langle\boldsymbol{\lambda}|\hat{\rho}(0)|\boldsymbol{\mu}\rangle|^2}{\langle\boldsymbol{\lambda}|\boldsymbol{\lambda}\rangle\langle\boldsymbol{\mu}|\boldsymbol{\mu}\rangle}\right|_{1\text{ph}}=\frac{h_1(\lambda_a,P;\boldsymbol{\lambda})}{L^2}e^{-Lf_1(\lambda_a,P;\boldsymbol{\lambda})},\tag{102}$$

where both h_1 and f_1 have regular expansions in $1/c$,

$$f_1=\frac{a_1}{cL}+\frac{a_2}{c^2}+\ldots,\qquad h_1=1+\frac{b_1}{c}+\ldots.\tag{103}$$

The leading terms in these expansions are then fixed by Eq. (99), and in particular, we have

$$a_2=\frac{DP^2}{3}-4P^2\int_{-\infty}^{\infty}d\mu\,\gamma_{-2}(\mu).\tag{104}$$

Here, the pair distribution function $\gamma_{-2}(\mu)$ is defined as follows (cf. Ref. [45]):

$$\lim_{L\to\infty}\frac{1}{L^3}\sum_{i\neq j}\frac{g(\lambda_i,\lambda_j)}{(\lambda_i-\lambda_j)^2}=\int_{-\infty}^{\infty}d\lambda\,g(\lambda,\lambda)\gamma_{-2}(\lambda),\tag{105}$$

where $g(\lambda,\mu)$ is any smooth function. Importantly, this quantity depends on details of the state $|\boldsymbol{\lambda}\rangle$ beyond its root density, namely, the joint PDF of pairs of Bethe roots. The simplest way of determining it is by reverting to the sum in Eq. (101). The fact that the expression for a_2 [Eq. (104)] involves the pair distribution function shows explicitly that the matrix elements (102) depend on details of the microstate $|\boldsymbol{\lambda}\rangle$ beyond the macrostate information encoded in the particle root density.

In order to exhibit the structure (102) more fully, we have determined the square of the one-particle-hole matrix elements up to $\mathcal{O}(c^{-4})$ in Appendix A. Exponentiating the resulting infrared divergences using the conjecture (102) results in

$$\begin{aligned}\left.\frac{|\langle\boldsymbol{\lambda}|\hat{\rho}(0)|\boldsymbol{\mu}\rangle|^2}{\langle\boldsymbol{\lambda}|\boldsymbol{\lambda}\rangle\langle\boldsymbol{\mu}|\boldsymbol{\mu}\rangle}\right|_{1\text{ph,res}}\approx&\frac{\alpha^2}{L^2(1+\frac{2}{cL})^2}\left[1-\frac{4P'}{cL}(\Gamma_{-1}-\tilde{\Gamma}_{-1})+\frac{8(P')^2}{c^2L^2}(\Gamma_{-1}-\tilde{\Gamma}_{-1})^2+\frac{4(P')^2}{c^2L^2}(\Gamma_{-2}+\tilde{\Gamma}_{-2})\right.\\&\left.-\frac{4\Gamma_2}{c^3L}-\frac{12P^2}{c^3L}+\frac{4P^3}{3c^3L}(\Gamma_{-1}-\tilde{\Gamma}_{-1})-\frac{16P^3}{3c^3L^3}[2(\Gamma_{-1}-\tilde{\Gamma}_{-1})^3+3(\Gamma_{-1}-\tilde{\Gamma}_{-1})(\Gamma_{-2}+\tilde{\Gamma}_{-2})+(\Gamma_{-3}-\tilde{\Gamma}_{-3})\right]\\&\times\exp\left[-\frac{P^2(N-1)}{3c^2}+\frac{4(P')^2}{c^2L^2}\sum_{\substack{i\neq j\\ i,j\neq a}}\frac{1}{\lambda_{ij}^2}+\frac{4P^2D(N-1)}{c^3}-\frac{4PD\Gamma_1}{c^3}-\frac{8}{c^3L}(\Gamma_1^2-N\Gamma_2)\right].\end{aligned}\tag{106}$$

Here, we have introduced shorthand notations,

$$\Gamma_n=\sum_{i\neq a}(\lambda_{i,a})^n,\qquad\tilde{\Gamma}_n=\sum_{i\neq a}(\lambda_{i,a}-P')^n.\tag{107}$$

We have verified numerically that the expression (106) provides a good approximation to the exact matrix element at large values of c in the regime $L>c$. This finding supports the conjecture (102). Some of this evidence is presented in Appendix A.

Comparing Eq. (106) with Eq. (102) and dropping terms that vanish in the thermodynamic limit, we have

$$\begin{aligned}f_1(\lambda_a,P;\boldsymbol{\lambda})=&\frac{P^2D}{3c^2}-\frac{4P'^2}{c^2L^3}\sum_{i\neq j}\frac{1}{\lambda_{ij}^2}-\frac{4P^2D^2}{c^3}\\&+\frac{4PD\Gamma_1}{Lc^3}+\frac{8}{c^3L^2}(\Gamma_1^2-N\Gamma_2)+\ldots.\end{aligned}\tag{108}$$

In order to consider asymptotically large systems, it is useful to express f_1 in terms of the particle and hole rapidities using

$$\lambda_p=\lambda_h+P'\left(1+\frac{2}{cL}\right)+\mathcal{O}(c^{-3}).\tag{109}$$

Assuming, for simplicity, that the root distribution function $\rho(\lambda)$ of the rapidities $\boldsymbol{\lambda}$ is an even function from here on, we have

$$\begin{aligned}f_1(\lambda_h,\lambda_p;\boldsymbol{\lambda})=&\frac{P^2}{c^2}\left[\frac{D}{3}-\frac{4D^2}{c}-\frac{4}{\alpha^2}\int d\mu\gamma_{-2}(\mu)\right]\\&-\frac{4D^2}{c^3}\lambda_h(\lambda_p-\lambda_h)-\frac{8D}{c^3}\int d\mu\mu^2\rho(\mu)\\&+o(L^0).\end{aligned}\tag{110}$$

Here, we retain the label $\boldsymbol{\lambda}$ in order to indicate that f_1 depends on properties of the ket $|\boldsymbol{\lambda}\rangle$ beyond those encoded in its root density $\rho(\lambda)$. In the large-L limit, the logarithm of the matrix elements (84) for our one-particle-hole excitation then becomes

$$\mathfrak{M}^{\rho}_{\boldsymbol{\lambda},\boldsymbol{\mu}} = f_1(\lambda_h, \lambda_p; \boldsymbol{\lambda}) + o(L^0). \tag{111}$$

We can now determine the probability distribution $P(z, Q)$ of $\mathfrak{M}^{\rho}_{\boldsymbol{\lambda},\boldsymbol{\mu}}|_{1\mathrm{ph}}$ at a fixed momentum transfer Q between the two states. To that end, we introduce a rapidity cutoff Λ that translates into a cutoff $I^{(L)}_{\max}$ for our Bethe integers; i.e., we consider only solutions of the Bethe equations such that all (half-odd) integers fulfill $|I_j| < I^{(L)}_{\max}$. We then define

$$P^{\eta}_L(z, Q) = \frac{1}{N_1}\sum_{I_p, I_h}\delta_\eta(z - \mathfrak{M}^{\rho}_{\boldsymbol{\lambda},\boldsymbol{\mu}})\delta_\eta\left(Q - \frac{2\pi(I_p - I_h)}{L}\right), \tag{112}$$

where N_1 is the total number of one-particle-hole excitations given the state $|\boldsymbol{\lambda}\rangle$ and $I^{(L)}_{\max}$. We are interested in the joint PDF

$$\mathrm{P}(z, Q) = \lim_{\eta\to 0}\lim_{L\to\infty} P^{\eta}_L(z, Q). \tag{113}$$

Turning sums into integrals in the thermodynamic limit gives

$$\mathrm{P}(z, Q) = \frac{1}{\mathcal{N}_\Lambda}\int_{-\Lambda}^{\Lambda} d\lambda\rho(\lambda)\int_{-\Lambda}^{\Lambda} d\mu\rho_h(\mu) \times \delta(z - f_1(\lambda, \mu; \boldsymbol{\lambda}))\,\delta(Q - 2\pi[z(\mu) + z(\lambda)]), \tag{114}$$

where $z(\lambda)$ is the counting function defined in Eq. (31) and

$$\mathcal{N}_\Lambda = \int_{-\Lambda}^{\Lambda} d\lambda\rho(\lambda)\int_{-\Lambda}^{\Lambda} d\mu\rho_h(\mu). \tag{115}$$

In order to proceed, we now use the approximation

$$2\pi[z(\mu) - z(\lambda)] = (\mu - \lambda)\alpha + \mathcal{O}(c^{-3}), \tag{116}$$

which allows us to carry out the integral over μ in an elementary fashion,

$$\mathrm{P}(z, Q) \approx \frac{1}{\alpha\mathcal{N}_\Lambda}\sum_n \frac{\rho_p(x_n)\rho_h(x_n + Q/\alpha)}{|f_1'(x_n, x_n + Q/\alpha)|}, \tag{117}$$

where the sum is over solutions $|x_n| < \Lambda$ to the equation

$$z - f_1(x_n, x_n + Q/\alpha; \boldsymbol{\lambda}) = 0. \tag{118}$$

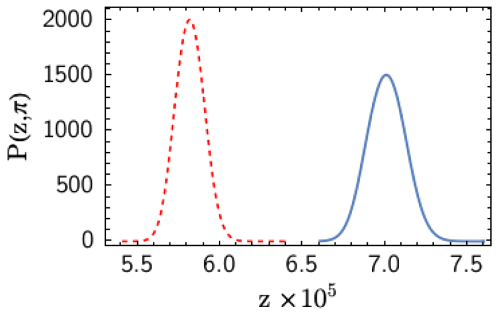

FIG. 20. Probability distribution functions $P(z, Q = \pi)$ for smooth microstates corresponding to thermal macrostates with $D = 0.25$, $\beta = 0.25$, $c = 100$ (blue), and $c = 110$ (red dashed).

In our case, there is only a single solution,

$$x_1(z, Q) = -\frac{zc^3\alpha}{4D^2Q} - \frac{2\alpha}{DQ}\int d\mu\mu^2\rho(\mu) + \frac{Qc}{4D^2\alpha}\left[\frac{D}{3} - \frac{4D^2}{c} - \frac{4}{\alpha^2}\int d\mu\gamma_{-2}(\mu)\right], \tag{119}$$

so we arrive at a very simple answer,

$$\mathrm{P}(z, Q) \approx \frac{c^3}{4D^2\mathcal{N}_\Lambda}\frac{\rho(x_1)\rho_h(x_1 + Q/\alpha)}{|Q|}. \tag{120}$$

The probability distribution functions $P(z, Q = \pi)$ for smooth microstates corresponding to a thermal macrostate with $D = 0.25$, $\beta = 0.25$ and two values of c are shown in Fig. 20. We see that, as expected, the probability distribution function narrows and peaks at smaller values of z as c is increased. In the limit $c \to \infty$, we know that $f_1 \to 0$.

Here, we have computed $\int d\mu\gamma_{-2}(\mu)$ by considering the scaling of its finite-size expression with L for large systems of up to $L = 4096$. It is important to stress that the thermodynamic limit result shown in Fig. 20 is approached only for very large L such that $Lf_1 \gg 1$. The results of this subsection are summarized as follows:

(i) Matrix elements involving a single-particle-hole excitation over a given microstate at a finite energy density relative to the ground state are exponentially small in system size,

$$\left.\frac{|\langle\boldsymbol{\lambda}|\hat{\rho}(0)|\boldsymbol{\mu}\rangle|^2}{\langle\boldsymbol{\lambda}|\boldsymbol{\lambda}\rangle\langle\boldsymbol{\mu}|\boldsymbol{\mu}\rangle}\right|_{1\mathrm{ph}} = \frac{h_1(\lambda_a, P; \boldsymbol{\lambda})}{L^2}e^{-Lf_1(\lambda_a, P; \boldsymbol{\lambda})}, \tag{121}$$

where the function f_1 depends on details of the microstate beyond the root density $\rho(\lambda)$ that specifies the macrostate to which it belongs. Above, we have derived explicit expressions for the $1/c$ expansions of the functions h_1 and f_1.

(ii) These matrix elements are very large compared to typical matrix elements in the same macrostate, which scale as Eq. (96).

(iii) If we introduce a momentum cutoff, there are only polynomially many (in system size) single-particle-hole excitations, which means that they do not contribute to the thermodynamic limit of Lehmann representations of two-point functions for the same reasons as discussed below Eq. (72).

2. Multiple-particle-hole excitations

We have verified numerically that making a fixed number of particle-hole excitations over a microstate belonging to a thermal macrostate again leads to matrix elements that are exponentially small in system size. Hence, such matrix elements are also anomalously large compared to typical ones. However, given a momentum cutoff, there are only polynomially many (in system size) m-particle-hole excitations (where m is fixed), which means that they do not contribute to the thermodynamic limit of Lehmann representations of two-point functions for the same reasons as discussed below Eq. (72). The states that contribute to such Lehmann representations involve an extensive number of particle-hole excitations.

VIII. SUMMARY AND CONCLUSIONS

In this work, we have used integrability methods to determine the structure of matrix elements of local operators in energy eigenstates of the Lieb-Liniger model. The latter is a key paradigm of integrable many-particle quantum systems and has the distinctive property that energy eigenstates at an arbitrary energy density can be understood in terms of a single species of elementary excitations, which greatly simplifies the task of numerically determining matrix elements for large system sizes. The existence of an extensive number of mutually compatible conserved charges affects the structure of energy eigenstates at finite energy densities: In addition to thermal states, we can have other macrostates that differ in their values of the densities of some of the conserved charges. Our results for the structure of matrix elements of local operators in the Lieb-Liniger model can be summarized as follows.

(i) Typical diagonal matrix elements in a macrostate characterized by a root density $\rho(\lambda)$ depend only on macrostate information up to finite-size corrections,

$$\frac{\langle \boldsymbol{\mu}|\mathcal{O}(0)|\boldsymbol{\mu}\rangle}{\langle \boldsymbol{\mu}|\boldsymbol{\mu}\rangle} = f_{\mathcal{O}}(\rho) + \mathcal{O}(L^{-\frac{1}{2}}). \tag{122}$$

Here, $f_{\mathcal{O}}(\rho)$ is a function that depends smoothly on the densities of the conserved charges, which can be thought of as a natural generalization of the eigenstate thermalization hypothesis for diagonal matrix elements. Our findings are in agreement with previous work on diagonal matrix elements in nonthermal states in the spin-1/2 XXZ chain [19].

(ii) Typical off-diagonal matrix elements involving microstates belonging to two different macrostates scale with system size as

$$\frac{|\langle \boldsymbol{\mu}|\mathcal{O}(0)|\boldsymbol{\lambda}\rangle|^2}{\langle \boldsymbol{\lambda}|\boldsymbol{\lambda}\rangle\langle \boldsymbol{\mu}|\boldsymbol{\mu}\rangle} \propto e^{-c^{\mathcal{O}}_{\rho_0,\rho_1} L^2}. \tag{123}$$

Here, $c^{\mathcal{O}}_{\rho_0,\rho_1}$ is a constant that depends on the macrostates under consideration and *a priori* on the operator $\mathcal{O}$.

(iii) Typical off-diagonal matrix elements involving microstates belonging to the same macrostate scale with system size as

$$\frac{|\langle \boldsymbol{\mu}|\mathcal{O}(0)|\boldsymbol{\lambda}\rangle|^2}{\langle \boldsymbol{\lambda}|\boldsymbol{\lambda}\rangle\langle \boldsymbol{\mu}|\boldsymbol{\mu}\rangle} \propto e^{-c^{\mathcal{O}}_0 L\ln(L) - L M^{\mathcal{O}}_{\boldsymbol{\lambda},\boldsymbol{\mu}}}, \tag{124}$$

where $c^{\mathcal{O}}_0$ depends on the macrostates under consideration as well as (*a priori*) on the operator $\mathcal{O}$. The PDF for $M^{\mathcal{O}}_{\boldsymbol{\lambda},\boldsymbol{\mu}}$, where we sample both $\boldsymbol{\lambda}$ and $\boldsymbol{\mu}$, is well described by a Fréchet distribution. If we fix the ket state $|\boldsymbol{\lambda}\rangle$ and consider the PDF of matrix elements obtained by sampling $|\boldsymbol{\mu}\rangle$, we observe a strong dependence on the details of $|\boldsymbol{\lambda}\rangle$, i.e., the multivariate probability distribution of half-odd integers. Nevertheless, if we fix $|\boldsymbol{\lambda}\rangle$ to be the smooth thermal state, the PDF for $M^{\mathcal{O}}_{\boldsymbol{\lambda},\boldsymbol{\mu}}$ is well characterized by a Fréchet distribution (with different parameters compared to the case where we sample both $\boldsymbol{\lambda}$ and $\boldsymbol{\mu}$).

(iv) There are rare, but still exponentially many (in particle number, given a momentum cutoff), matrix elements between eigenstates that belong to the same macrostate that are much larger than Eq. (124) but are instead merely exponentially small in system size,

$$\left.\frac{|\langle \boldsymbol{\mu}|\mathcal{O}(0)|\boldsymbol{\lambda}\rangle|^2}{\langle \boldsymbol{\lambda}|\boldsymbol{\lambda}\rangle\langle \boldsymbol{\mu}|\boldsymbol{\mu}\rangle}\right|_{\text{rare}} \propto e^{-L M^{\mathcal{O}}_{\boldsymbol{\lambda},\boldsymbol{\mu}}}. \tag{125}$$

These matrix elements can be characterized by the property that the sets of (half-odd) integers corresponding to the Bethe roots $\boldsymbol{\lambda}$ and $\boldsymbol{\mu}$ are atypically close to one another. For the case of the density operator, we obtain explicit results for the simplest such matrix elements by generalizing the $1/c$-expansion method pioneered in Refs. [45,55].

(v) The observed structure of off-diagonal matrix elements in interacting theories is very similar to the one we find for the Bose field in the $c \to \infty$ limit, in which the Lieb-Liniger model can be mapped to free fermions. The origin of this similarity is the structure of the singularities of the matrix elements when viewed as functions of the spectral parameters (in a large finite volume, the fact that the spectral

parameters must fulfill the Bethe equations regularizes these singularities).

Our work poses a number of important questions that should be addressed in future work. First and foremost, it should be clarified whether the results obtained here indeed carry over to all local operators in the Lieb-Liniger model, and to other integrable models, as we conjecture. To that end, it would be useful to consider nonthermal macrostates in the spin-1/2 XXZ chain as was done in Ref. [19] and check whether the same kind of scaling behavior of matrix elements with system size reported here occurs. An analysis of the matrix elements of the Bose field in the Lieb-Liniger model for $0 < c < \infty$ will be reported elsewhere [70]. Second, one should attempt to conduct an analogous study in models that feature bound states (string solutions to the Bethe equations). This case appears difficult at present and will require better control of matrix elements involving strings than is available in the literature. Third, the statistical properties of the rare, large matrix elements should be investigated in more detail in the case where one has a finite but low density of particle-hole excitations. Here, the hope is to find a way to randomly sample the large matrix elements that dominate the Lehmann representations of two-point functions and related quantities of interest [71].

ACKNOWLEDGMENTS

We are very grateful to J.-S. Caux and N. Robinson for collaborating with us during the early stages of this work and for numerous very helpful discussions and suggestions. This research was funded in part by the UKRI under Grant No. EP/S020527/1 (F. H. L. E.) and the European Research Council under ERC Advanced Grant No. 743032 DYNAMINT (A. J. J. M.dK.).

F. H. L. E. conceptualized the work, carried out all calculations and computations, and wrote the manuscript. A. J. J. M. dK. worked on carrying out numerical calculations for the interacting case and analyzing the associated results.

APPENDIX A: $1/c$ EXPANSION OF THE ONE-PARTICLE-HOLE MATRIX ELEMENT

In this appendix, we present some details regarding the $1/c$ expansion of the density matrix element (84) between two Bethe states differing by a single-particle-hole excitation, cf. Sec. VII C 1 of the main text. For convenience, we first recall some of the notations introduced in the main text. We consider two solutions, $\boldsymbol{\lambda}$ and $\boldsymbol{\mu}$, to the Bethe ansatz equations, with corresponding sets of (distinct) integers $\{I_j\}$ and $\{J_j\}$, where

$$J_j = I_j, \qquad j \neq a, \qquad J_a = I_a + n. \tag{A1}$$

This case corresponds to a hole with integer I_a (rapidity λ_a) and a particle with integer $I_a + n$ (rapidity μ_a). The momentum difference between the two states is $P = 2\pi n/L$. In order to simply the expression for the matrix element in the $1/c$ expansion, it is useful to introduce short-hand notation,

$$\lambda_{i,j} = \lambda_i - \lambda_j, \qquad \alpha = 1 + \frac{2D}{c}, \qquad P' = \frac{P}{\alpha},$$
$$\Gamma_n = \sum_{i\neq a} (\lambda_{i,a})^n, \qquad \tilde{\Gamma}_n = \sum_{i\neq a} (\lambda_{i,a} - P')^n. \tag{A2}$$

Solving the Bethe equations in the framework of the $1/c$ expansion gives

$$\lambda_i = \frac{2\pi I_i}{\alpha L} + \frac{4\pi}{cL^2\alpha}\sum_{j=1}^{N} I_j + \frac{(2\pi)^4}{3\pi c^3(\alpha L)^4}\sum_{j=1}^{N}(I_i - I_j)^3 + \mathcal{O}(c^{-4}). \tag{A3}$$

Then, we can express the rapidities μ_k in terms of λ_j as

$$\mu_i = \lambda_i + \frac{2P'}{cL}\left[1 - \frac{(\lambda_{i,a})^2}{c^2} + \frac{P\lambda_{i,a}}{c^2} - \frac{P^2}{3c^2}\right] + \mathcal{O}(c^{-4}),$$
$$\mu_a = \lambda_a + P'\left[1 + \frac{2}{cL}\right] + \frac{2}{3c^3 L}\sum_{k\neq a}[(\lambda_{a,k} + P)^3 - \lambda_{a,k}^3] + \mathcal{O}(c^{-4}). \tag{A4}$$

We now extend the analysis of Ref. [45] by carrying out a $1/c$ expansion of the various factors in the expression (81) of the matrix elements of the density operator up to order $\mathcal{O}(c^{-4})$. As in Ref. [45], we retain certain contributions to all orders. We find

$$A_1 \equiv \prod_{i\neq j}\frac{\lambda_{i,j} + ic}{\mu_{i,j} + ic} \simeq 1 - \frac{P'^2(N-1)}{c^2} + \frac{2P'}{c^2}\Gamma_1(\lambda_a),$$
$$A_2 \equiv \left|\prod_{i\neq a}(V_i^+ - V_i^-)\right|^2 \simeq \left(\frac{2P}{c}\right)^{2N-2}\left(1 - \frac{2}{c^2}\Gamma_2(\lambda_a)\right),$$
$$A_3 \equiv \prod_{\substack{i\neq j\\ i\neq a\\ j\neq a}}\frac{\lambda_{i,j}\mu_{i,j}}{(\lambda_i - \mu_j)^2} \simeq 1 + \frac{4P'^2}{c^2L^2}\sum_{\substack{i\neq j\\ i\neq a\\ j\neq a}}\frac{1}{\lambda_{i,j}^2},$$
$$\mathcal{N}_{\boldsymbol{\lambda}} \simeq \alpha^{N-1}\left[1 + \frac{4}{c^3 L}\left(\left(\sum_i \lambda_i\right)^2 - N\sum_i \lambda_i^2\right)\right],$$
$$\mathcal{N}_{\boldsymbol{\mu}} \simeq \mathcal{N}_{\boldsymbol{\lambda}}\left[1 + \frac{4P}{c^3 L}(2\Gamma_1(\lambda_a) - (N-1)P)\right], \tag{A5}$$

$$A_4 \equiv \prod_{i\neq a}\frac{\lambda_{i,a}^2}{(\mu_i-\lambda_a)^2} \simeq 1-\frac{4P'}{cL}\Gamma_{-1}+\frac{8P'^2}{c^2L^2}\left[\Gamma_{-1}^2+\frac{\Gamma_{-2}}{2}\right] -\frac{16P^3}{3c^3L^3}[2\Gamma_{-1}^3+3\Gamma_{-1}\Gamma_{-2}+\Gamma_{-3}] +\frac{4P}{c^3L}\left[\Gamma_1-3P+\frac{P^2\Gamma_{-1}}{3}\right]. \tag{A6}$$

$$A_5 \equiv \prod_{i\neq a}\frac{(\mu_i-\mu_a)^2}{(\lambda_i-\mu_a)^2} \simeq 1+\frac{4P'}{cL}\left(1-\frac{P^2}{3c^2}\right)\tilde{\Gamma}_{-1} +\frac{4P'^2}{c^2L^2}[2\tilde{\Gamma}_{-1}^2+\tilde{\Gamma}_{-2}]-\frac{4P}{Lc^3}\Gamma_1 +\frac{16P^3}{3c^3L^3}[2\tilde{\Gamma}_{-1}^3+3\tilde{\Gamma}_{-2}\tilde{\Gamma}_{-1}+\tilde{\Gamma}_{-3})], \tag{A7}$$

$$A_6 \equiv \prod_{i=1}^{N}\frac{1}{(\lambda_i-\mu_i)^2} \simeq \frac{\alpha^{2N}}{P^2}\left(\frac{Lc}{2P}\right)^{2N-2} \times\left[1+\frac{2}{c^2}\left(\Gamma_2-P\Gamma_1+\frac{P^2}{3}(N-1)\right)\left(1-\frac{2}{cL}\right)\right]. \tag{A8}$$

Finally, we have

$$i(\mu_l-\lambda_l)\prod_{k\neq l}\frac{\mu_k-\lambda_l}{\lambda_k-\lambda_l}\left[\frac{2c}{\lambda_{l,j}^2+c^2}-\frac{2c}{(\lambda_{p,j}^2+c^2}\right]\simeq 0, \qquad \left(\sum_i \mu_i-\lambda_i\right)^2\simeq P^2. \tag{A9}$$

The leading corrections in Eqs. (A5)–(A9) are of order $\mathcal{O}(c^{-4})$. Substituting the results back into the expression (84) for the matrix elements leads to the following expression for states that differ by a single-particle-hole excitation,

$$\left.\frac{|\langle\boldsymbol{\lambda}|\hat{\rho}(0)|\boldsymbol{\mu}\rangle|^2}{\langle\boldsymbol{\lambda}|\boldsymbol{\lambda}\rangle\langle\boldsymbol{\mu}|\boldsymbol{\mu}\rangle}\right|_{1\mathrm{ph}} = \frac{\alpha^2}{L^2(1+\frac{2}{cL})^2}\left[1-\frac{4P'}{cL}(\Gamma_{-1}-\tilde{\Gamma}_{-1})-\frac{P^2(N-1)}{3c^2}+\frac{4P'^2}{c^2L^2}\sum_{i\neq j}\frac{1}{\lambda_{ij}^2}+\frac{8P'^2}{c^2L^2}(\Gamma_{-1}-\tilde{\Gamma}_{-1})^2 +\frac{4P'^2}{c^2L^2}(\Gamma_{-2}+\tilde{\Gamma}_{-2})+\frac{4P^3N}{3c^3L}(\Gamma_{-1}-\tilde{\Gamma}_{-1})+\frac{4P^2D(N-1)}{c^3}-\frac{4PD\Gamma_1}{c^3}-\frac{4\Gamma_2}{c^3L} -\frac{8}{c^3L}\left(\left(\sum_i\lambda_i\right)^2-N\sum_i\lambda_i^2\right)-\frac{12P^2}{c^3L}-\frac{16P^3}{3c^3L^3}[2(\Gamma_{-1}-\tilde{\Gamma}_{-1})^3+3(\Gamma_{-1}-\tilde{\Gamma}_{-1})(\Gamma_{-2}+\tilde{\Gamma}_{-2}) +(\Gamma_{-3}-\tilde{\Gamma}_{-3})]-\frac{16P^3}{c^3L^3}(\Gamma_{-1}-\tilde{\Gamma}_{-1})\sum_{i\neq j}\frac{1}{\lambda_{ij}^2}\Bigg]+\mathcal{O}(c^{-4}). \tag{A10}$$

This expression indeed exhibits "infrared divergences," i.e., contributions that acquire additional factors of L compared to the leading term, which are compatible with Eq. (102). We conjecture that these terms can be exponentiated, and in order to do so, it is useful to return to the individual factors they arise from:

$$A_1\approx A_1^{(\mathrm{r})}=\exp\left(-\frac{P'^2(N-1)}{c^2}+\frac{2P'}{c^2}\Gamma_1\right),$$
$$A_2\approx A_2^{(\mathrm{r})}=\left(\frac{2P}{c}\right)^{2N-2}\exp\left(-\frac{2}{c^2}\Gamma_2\right),$$
$$A_3\approx A_3^{(\mathrm{r})}=\exp\left(\frac{4P'^2}{c^2L^2}\sum_{\substack{i\neq j\\ i,j\neq a}}\frac{1}{\lambda_{i,j}^2}\right),$$
$$\mathcal{N}_{\boldsymbol{\lambda}}\approx\mathcal{N}_{\boldsymbol{\lambda}}^{(\mathrm{r})}=\alpha^{N-1}\exp\left(\frac{4}{c^3L}(\Gamma_1^2-N\Gamma_2)\right), \tag{A11}$$

$$A_6\approx A_6^{(\mathrm{r})} = \frac{\alpha^{2N}}{P^2(1+\frac{2}{cL})^2}\left(\frac{Lc}{2P}\right)^{2N-2} \times\exp\left(\frac{2}{c^2}\left(\Gamma_2-P\Gamma_1+\frac{P^2}{3}(N-1)\right)\left(1-\frac{2}{cL}\right)\right). \tag{A12}$$

Using Eqs. (A11) and (A12) to exponentiate the infrared singularities in Eq. (A10) results in the expression (106) in the main text. In order to assess the accuracy of Eq. (106), we have computed its ratio R to numerically exact matrix elements for a number of particle-hole excitations over a "smooth" thermal state with $\beta=1$, where

$$R=\left.\frac{|\langle\boldsymbol{\lambda}|\hat{\rho}(0)|\boldsymbol{\mu}\rangle|^2}{\langle\boldsymbol{\lambda}|\boldsymbol{\lambda}\rangle\langle\boldsymbol{\mu}|\boldsymbol{\mu}\rangle}\right|_{1\mathrm{ph,res}}\left(\left.\frac{|\langle\boldsymbol{\lambda}|\hat{\rho}(0)|\boldsymbol{\mu}\rangle|^2}{\langle\boldsymbol{\lambda}|\boldsymbol{\lambda}\rangle\langle\boldsymbol{\mu}|\boldsymbol{\mu}\rangle}\right|_{1\mathrm{ph}}\right)^{-1}. \tag{A13}$$

TABLE I. Results for the ratios of the resummed $1/c$ expansions for matrix elements to the numerically exact results for $c = 100$, $L = N = 128$, and $\beta = 1$. We see that the resummed expression works rather well. As expected, it becomes worse when the excited state involves larger differences $|\lambda_p - \lambda_h|$ as the $1/c$ expansion requires these to be small compared to c.

P	$2J_a$	$2I_a$	$A_1^{(r)}/A_1$	$A_2^{(r)}/A_2$	$A_3^{(r)}/A_3$	$A_6^{(r)}/A_6$	R
−5.15	−287	−77	0.998	1.00	1.03	0.995	1.022
−3.14	−261	−133	0.999	1.00	1.02	0.991	1.014
5.35	223	5	0.999	1.00	1.02	1	1.018
−4.47	−173	9	1.00	1.00	1.01	1	1.013
4.57	207	21	0.999	1.00	1.01	1.00	1.015
−2.85	−155	−39	1.00	1.00	1.01	1	1.009
−6.92	−243	39	0.999	1.00	1.02	1	1.025
6.97	273	−11	0.998	1.00	1.02	1.00	1.027
−6.38	−225	35	0.999	1.00	1.02	1	1.021
−4.61	219	−31	0.999	1.00	1.02	1	1.016

For the same states, we have also checked the accuracy of the exponentiations (A11) and (A12). Results for $L = N = 128$ and $c = 100$ are shown in Table I. We see that the results are quite satisfactory. The values of β and c have been chosen to ensure that the differences $|\lambda_{j,k}|$ are all small compared to c, which is a key assumption of the $1/c$ expansion, cf. the discussion in Ref. [45]. We note that the factors $A_n^{(r)}$ are generally quite different from their "bare" values, which indicates the breakdown of the bare $1/c$ expansion. However, in the final expression (106), a number of cancellations occur, which render the resummed result (106) very close to the bare expression (A10) for the parameters considered here.

APPENDIX B: SAMPLING MACROSTATES IN A FINITE VOLUME

In this appendix, we discuss in some detail how to sample a given macrostate for a large, finite number of particles. The key element is to generate appropriate sets of "Bethe integers" I_j, which characterize the solutions of the Bethe equations (27). For simplicity, we focus on the impenetrable case $c = \infty$, where

$$\lambda_j = \frac{2\pi I_j}{L}. \tag{B1}$$

Thermal states are of particular interest as they are the most abundant states at a given energy density, and we therefore focus on them in our discussion. The generalization to atypical finite entropy density states is straightforward. To be specific, we take $c = \infty$ and consider a temperature $T = 10$ and chemical potential $\mu = 12.1058$. This approach gives particle density $D = 1$, energy density

$$e_\infty = 8.036608362699118, \tag{B2}$$

and root density

$$\rho(x) = \frac{1}{2\pi}\frac{1}{1 + e^{(x^2-\mu)/T}}. \tag{B3}$$

The corresponding density of I_j/L is simply

$$\varrho(\nu) = \frac{1}{1 + e^{((2\pi\nu)^2-\mu)/T}}. \tag{B4}$$

For later convenience, we define a cumulative probability distribution function

$$C(\nu) = \frac{1}{D}\int_0^\nu d\nu' \varrho(\nu'). \tag{B5}$$

1. Microcanonical ensemble

Let us start by randomly sampling distinct integers and just fixing an energy window for "acceptable states." We now fix our particle number and system size to $N = L = 32$ and consider energies in the window

$$|E - e_\infty L| < 2. \tag{B6}$$

In order to be able to sample energy eigenstates, we also need to impose the constraint

$$|I_j| < I_{\max}, \tag{B7}$$

where the values of $I_{\max}$ we have considered are $I_{\max} \leq 36$. The cutoff (B7) is required as the numerical cost for finding configurations that fulfill Eq. (B6) increases exponentially with N. The histogram of integers occurring in eigenstates fulfilling this constraint is shown in Fig. 21. We see that our microcanonical ensemble nicely reproduces the thermodynamic root density (B4). In Figs. 22 and 23, we show results for the probability distributions of total momentum and the third conservation law

$$\nu_\lambda^{(1)} = \sum_{n=1}^{32}\lambda_n, \qquad \nu_\lambda^{(3)} = \sum_{n=1}^{32}\lambda_n^3 \tag{B8}$$

in the microcanonical ensemble.

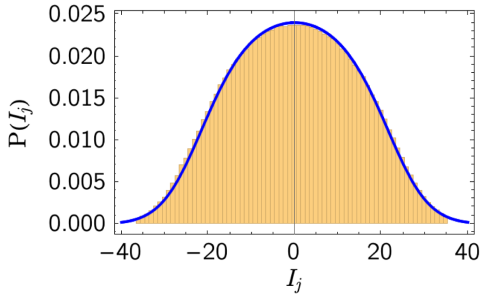

FIG. 21. Histogram of integers occurring in the microcanonical ensemble (B6). The blue curve is the thermodynamic root distribution function $(1/L)\varrho(I/L)$.

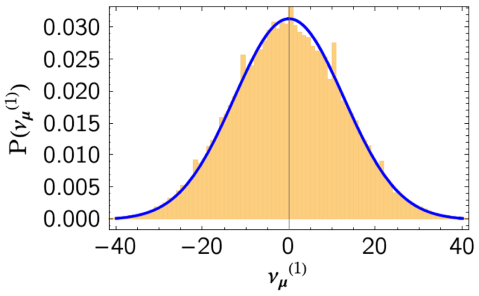

FIG. 22. Histogram of the total momentum in the microcanonical ensemble (B6). The curve is a fit to a normal distribution.

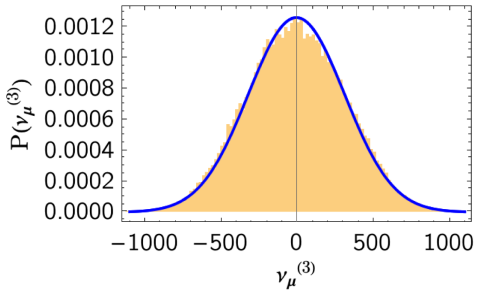

FIG. 23. Histogram of the eigenvalues of the third conservation law in the microcanonical ensemble (B6). The curve is a fit to a normal distribution.

The averages for these conserved quantities are, as expected, zero, but the spread of eigenvalues is very large. Finally, we show the probability distribution of the matrix elements of the Bose field $\mathfrak{M}_{\lambda,\mu}$ [Eq. (63)] in Fig. 24. The microcanonical sampling described here cannot be used for large particle numbers because it is extremely inefficient. The set of half-odd integer numbers we need to sample has dimension

$$\binom{2I_{\max}}{N}, \tag{B9}$$

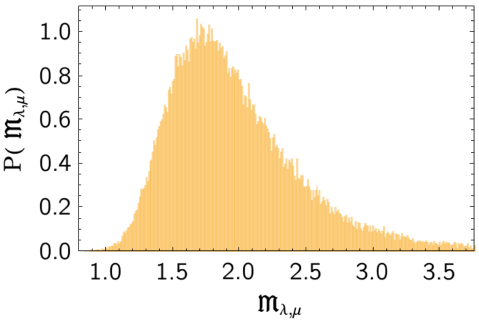

FIG. 24. Histogram of the logarithm of matrix elements $\mathfrak{M}_{\lambda,\mu}$ [Eq. (63)] between the smooth ket state and bra states obtained by microcanonical sampling (B6).

which grows exponentially with the number of particles. We therefore require more efficient ways of sampling the relevant microstates.

2. Plain vanilla box sampling (PVBS)

The simplest idea for targeting energy eigenstates in the appropriate energy window is to use "box sampling" of the probability distribution $\varrho(\nu)/D$. The rationale behind this approach is that, for very large numbers of particles, almost all these states will correspond to a discretization of $\varrho(\nu)$, cf. the steps leading to our expression for the entropy (16). Thus, we approximate $\varrho(\nu)$ as shown in Fig. 25. To that end, we introduce a cutoff a_0 (which corresponds to $-I_{\max}$ in the discussion of the microcanonical ensemble in the previous subsection) and then subdivide the ν axis into intervals $B_n = [a_{n-1}, a_n]$ for $1 \le n \le M$. The density of $\nu_j = I_j/L$ in B_n is then taken to be

$$\varrho_n \equiv D[C(a_n) - C(a_{n-1})], \tag{B10}$$

where the cumulative PDF $C(\nu)$ is defined in Eq. (B5). We can straightforwardly translate this solution into a distribution function of (half-odd) integers that is piecewise constant on the M intervals,

$$\bar{B}_n = [J_{n-1}, J_n). \tag{B11}$$

The number of integers in box $\bar{B}_n$ is $J_n - J_{n-1}$, where, in practice, we adjust a_0 in such a way that

$$\sum_{n=1}^{M} N_n = N = DL. \tag{B12}$$

We now sample the discretized probability distribution box by box: From the (half-odd) integers in $\bar{B}_n$, we randomly select N_n elements, where

$$N_n = \mathrm{Round}(L\varrho_n). \tag{B13}$$

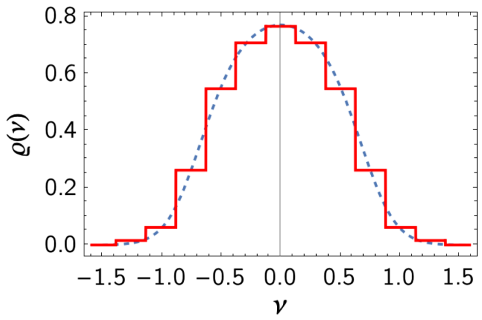

FIG. 25. Discretization of the distribution function $\varrho(\nu)$.

The total number of different configurations in the resulting sample space is

$$\mathfrak{N}_M(\{N_j\}) = \prod_{n=1}^{M} \binom{J_n - J_{n-1}}{N_n} \equiv e^{L\mathfrak{s}_M}. \quad \text{(B14)}$$

This number is much smaller than the number of configurations that need to be sampled in the microcanonical ensemble discussed earlier, which corresponds to the choice $M = 1$. Importantly, in the double limit

$$\lim_{M\to\infty} \lim_{L\to\infty} \mathfrak{s}_M, \quad \text{(B15)}$$

the number of microstates produced by this procedure recovers the correct entropy density of the thermal macrostate under consideration. One may therefore expect that this procedure provides a good way of sampling thermal states in finite systems. For a finite number of particles, the number of sampled states decreases with M, and in our example, we find

$$\mathfrak{s}_3 = 1.04, \qquad \mathfrak{s}_5 = 1.01, \qquad \mathfrak{s}_7 = 0.952773. \quad \text{(B16)}$$

These values should be compared with the thermodynamic result 1.20041. In practice, we still need to impose the energy-window restriction (B6) so that the actual number of states is smaller. For the finite particle numbers of relevance here, PVBS does not agree well with the microcanonical sampling. To show the degree of difference, we present results for $M = 7$ and our $L = N = 32$ example. In Fig. 26, we show the distribution of integers, which reproduces the thermodynamic root distribution function in a satisfactory manner.

In Figs. 27 and 28, we show the distribution of the total momentum and third conservation laws, respectively. We observe that both distributions are considerably narrower than the corresponding ones for microcanonical sampling; see Figs. 22 and 23. Finally, we show the probability distribution of the matrix elements of the Bose

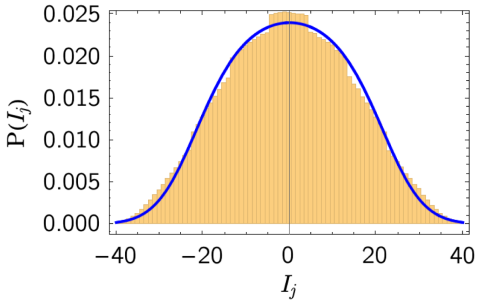

FIG. 26. Histogram of integers obtained by PVBS with $M = 7$. The blue curve is the thermodynamic root distribution function $(1/L)\varrho(I/L)$.

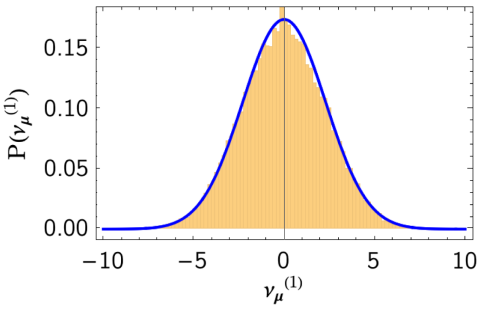

FIG. 27. Histogram of the total momentum obtained by PVBS with $M = 7$. The curve is a fit to a normal distribution.

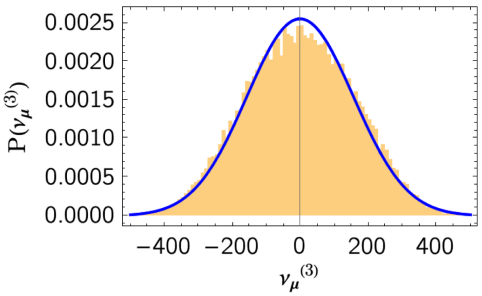

FIG. 28. Histogram of the eigenvalues of the third conservation law obtained by PVBS with $M = 7$. The curve is a fit to a normal distribution.

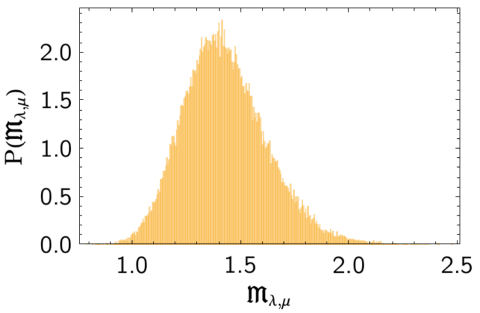

FIG. 29. Histogram of the logarithm of matrix elements $\mathfrak{M}_{\lambda,\mu}$ [Eq. (63)] between the smooth ket state and bra states obtained by PVBS with $M = 7$.

field $\mathfrak{M}_{\lambda,\mu}$ [Eq. (63)] in Fig. 29. We observe that the typical matrix elements obtained by PVBS are significantly larger than in microcanonical sampling, cf. Fig. 24. The differences in the probability distributions of matrix elements and the eigenvalues of conserved quantities between PVBS and MC sampling are easy to understand intuitively: By construction, PVBS produces significantly smaller fluctuations than the MCE in finite volumes. While the expectation is that these finite-size effects will disappear as the thermodynamic limit is approached, they severely limit the utility of PVBS for the (numerically) accessible system sizes.

3. Fluctuating box sampling

As we have seen, in mesoscopic volumes, the PVBS accesses a much more restrictive set of energy eigenstates than the MCE. We can make up for this difference by allowing the box occupation numbers N_n to fluctuate. Given a set B of boxes with vacancies $(V_1, \ldots, V_M)$, we generate a set of occupation numbers $\{N_j\}$ such that

$$\sum_j N_j = N, \tag{B17}$$

where we allow the N_j to fluctuate as follows. Let $N_j^{(\mathrm{PV})}$ be the PVBS particle numbers. We then take

$$N_j = N_j^{(\mathrm{PV})} + \delta N_j, \tag{B18}$$

where the random integers δN_j are taken to add up to zero and fulfill

$$\delta N_j = \mathcal{O}\left(\min\left\{\sqrt{N_j^{(\mathrm{PV})}}, \sqrt{|V_j - N_j^{(\mathrm{PV})}|}\right\}\right). \tag{B19}$$

Given a set of particle numbers $(N_1, \ldots, N_M)$, we calculate the number of microstates obtained by box sampling,

$$\mathfrak{N}_M(\{N_j\}, \{V_j\}) = \prod_{n=1}^{M} \binom{V_n}{N_n}. \tag{B20}$$

We then generate

$$\left[\frac{\mathfrak{N}_M(\{N_j\}, \{V_j\})}{N_0}\right] \tag{B21}$$

samples from the configuration specified by $\{N_1, \ldots, N_M\}$, where N_0 is some fixed reference number. By construction, this procedure increases fluctuations. In practice, we may choose the outermost boxes to be larger in order to decrease "tail effects." Results obtained by this method for $N = L = 32$ are shown in Figs. 30–33.

We see that the fluctuating box sampling (FBS) reproduces the results of the MCE fairly well. However, this method requires that the fluctuations are taken to be sufficiently strong. In particular, if we make them weaker by changing the coefficient that multiplies the rhs in the expression for δN_j, the agreement becomes worse. This result is as expected. FBS is significantly slower than PVBS and becomes computationally very expensive for large particle numbers.

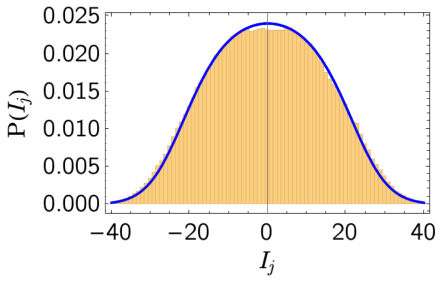

FIG. 30. Histograms of integers produced by FBS with $M = 7$ and energies in the window $|E - e_\infty L| < 2$.

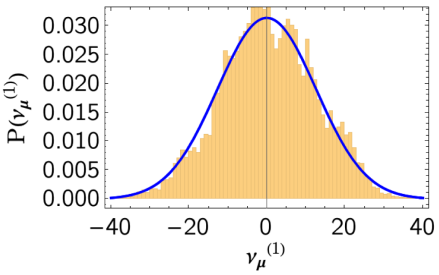

FIG. 31. Histograms of momentum produced by FBS with $M = 7$ compared to the MCE (solid blue line).

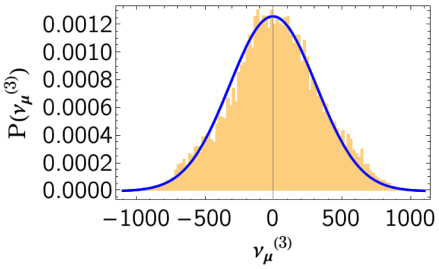

FIG. 32. Histograms of $\nu_\lambda^{(3)}$ produced by FBS with $M = 7$ compared to the MCE (solid blue line).

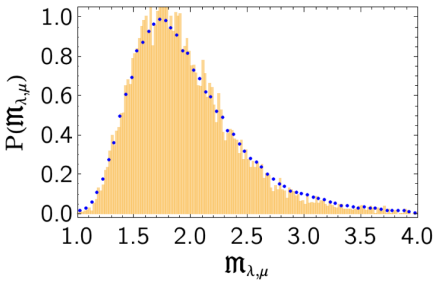

FIG. 33. Histogram of the matrix elements between the smooth "ket" state and energy eigenstates in the window $|E - e_\infty L| < 2$ obtained by FBS (yellow) and in the microcanonical ensemble (blue dots).

4. Random sampling (RS)

The distribution of integers in the microcanonical ensemble is well described by the thermodynamic distribution function $\varrho(\nu)/D$, which suggests that a random sampling of this probability distribution should reproduce the MCE. The difficulty is that we must generate *nonrepeating* integers. Our starting point is the set of integers

$$S_M = \{j | -I_{\max} \le j \le I_{\max}\}, \quad M = 2I_{\max} + 1, \tag{B22}$$

and an associated discrete probability distribution

$$P_M = \{p_1, \ldots, p_M\}. \tag{B23}$$

In practice, we take P_M to be a discretization of self-consistently determined continuous PDFs $P(\nu)$. The corresponding set of cumulative probabilities is

$$\mathcal{C}_M = \left\{ C_n = \sum_{j=1}^{n-1} p_j, n = 1, \ldots, 2I_{\max} + 2 \right\}. \tag{B24}$$

We now generate a (real) random number r in the interval $[0, 1]$ and determine the integer j such that

$$C_{j-1} < r < C_j. \tag{B25}$$

We then remove the integer j from the set S_M and define a new discrete probability distribution

$$P_{M-1} = \left\{ \frac{p_1}{1-p_j}, \ldots, \frac{p_{j-1}}{1-p_j}, \frac{p_{j+1}}{1-p_j}, \ldots, \frac{p_M}{1-p_j} \right\} \tag{B26}$$

and the associated cumulative probability distribution $\mathcal{C}_{M-1}$. Repeating this procedure N times results in a set of distinct integers $\{I_1, \ldots, I_N\}$. Finally, we impose that the probability distribution of these sets of integers is a discretization of the (normalized) root density $\varrho(\nu)/D$. Importantly, this case requires an initial probability distribution $P(\nu)$ that is different from $\varrho(\nu/D)$. The PDF required to produce the normalized root distribution upon random sampling is shown in the main text in Fig. 2. The corresponding distribution of integers is shown in Fig. 34. In Figs. 35–37, we show the histograms obtained by our random sampling procedure for the eigenvalues of momentum, the third conservation law, and the matrix elements of the Bose field operator between the smooth ket state and energy eigenstates in the window $|E - e_\infty L| < 2$.

We observe that the results are in good agreement with those obtained by microcanonical sampling. We conjecture that the remaining differences, in particular, in $P(\nu_\mu^{(3)})$, are at least partially caused by the cutoff in the MC sampling procedure.

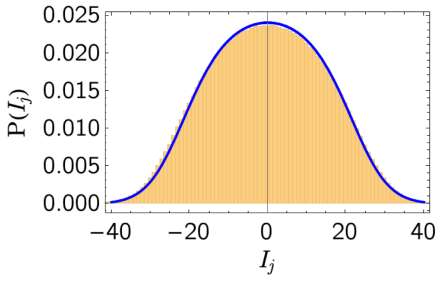

FIG. 34. Histogram of integers by RS using the probability distribution $P(\nu)$ shown in Fig. 2. The solid curve is the root distribution function $\varrho(\nu)/D$.

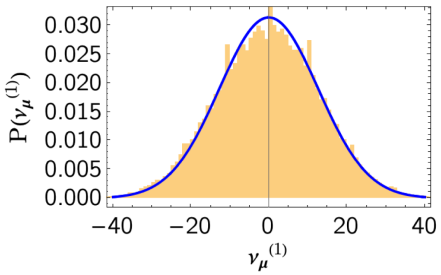

FIG. 35. Histograms of the total momentum obtained by RS under the constraint that $|E - e_\infty L| < 2$ for $N = L = 32$. The results in the microcanonical ensemble are shown as the solid blue line.

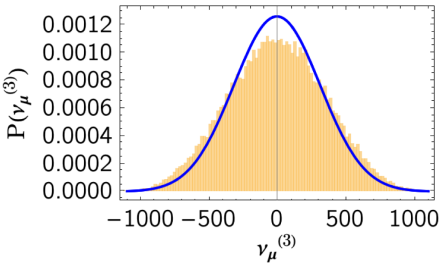

FIG. 36. Histograms of the third conservation law obtained by RS under the constraint that $|E - e_\infty L| < 2$ for $N = L = 32$. The results in the microcanonical ensemble are shown as the solid blue line.

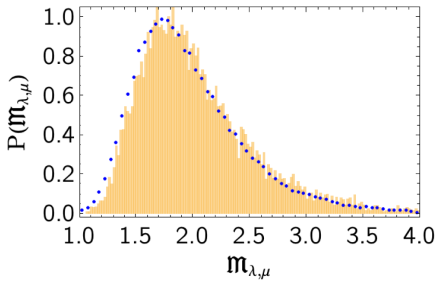

FIG. 37. Histograms of the matrix elements of the Bose field operator between the smooth ket state and energy eigenstates in the window $|E - e_\infty L| < 2$ for $N = L = 32$ obtained by RS (yellow) and in the microcanonical ensemble (blue dots).

5. Simplified random sampling (SRS)

The random sampling algorithm described above is somewhat slow. We therefore use the simplified algorithm described in Sec. III A of the main text. The latter is faster as it treats the constraint that all (half-odd) integers must be distinct in a much simpler fashion. It nevertheless gives results that agree with RS within the statistical error in all cases we have tested. Examples are shown in Figs. 38–40. Here, we have chosen a larger energy window $|E - e_\infty L| < 10$.

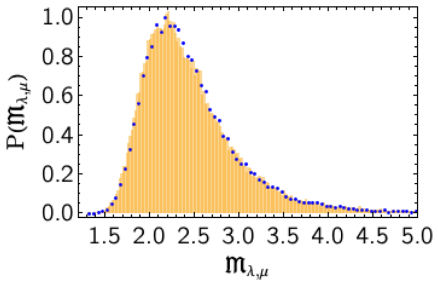

FIG. 38. Histogram of the matrix elements of the Bose field operator between the smooth ket state and energy eigenstates in the window $|E - e_\infty L| < 10$ obtained by SRS (yellow), and the analogous result for RS (blue dots).

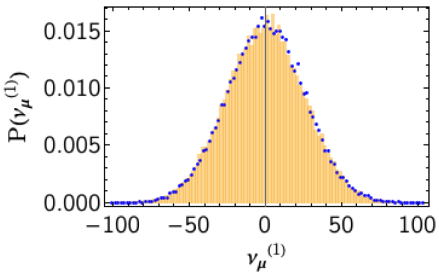

FIG. 39. Histogram of the eigenvalues of momentum for energy eigenstates in the window $|E - e_\infty L| < 10$ obtained by SRS (yellow), and the analogous result for RS (blue dots).

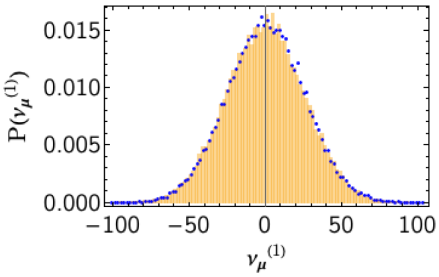

FIG. 40. Histogram of the eigenvalues of the third conservation law for energy eigenstates in the window $|E - e_\infty L| < 10$ obtained by SRS (yellow), and the analogous result for RS (blue dots).

6. Interacting case

As all sampling methods discussed above are based on drawing sets of nonrepeating (half-odd) integers $\{I_j\}$ from a probability distribution, they can be generalized, in a straightforward way, to the interacting case. The main differences are as follows:

(i) The target PDF $P(I_j)$ is obtained from Eq. (38) by solving the nonlinear integral equations (37) (for thermal macrostates).

(ii) For $0 < c < \infty$, we need to (numerically) solve the Bethe equations once we have generated a set $\{I_j\}$.

[1] J. M. Deutsch, *Quantum statistical mechanics in a closed system*, Phys. Rev. A **43**, 2046 (1991).
[2] M. Srednicki, *Chaos and quantum thermalization*, Phys. Rev. E **50**, 888 (1994).
[3] M. Srednicki, *The approach to thermal equilibrium in quantized chaotic systems*, J. Phys. A **32**, 1163 (1999).
[4] L. D'Alessio, Y. Kafri, A. Polkovnikov, and M. Rigol, *From quantum chaos and eigenstate thermalization to statistical mechanics and thermodynamics*, Adv. Phys. **65**, 239 (2016).
[5] M. Rigol, V. Dunjko, and M. Olshanii, *Thermalization and its mechanism for generic isolated quantum systems*, Nature (London) **452**, 854 (2008).
[6] M. Rigol and L. F. Santos, *Quantum chaos and thermalization in gapped systems*, Phys. Rev. A **82**, 011604(R) (2010).
[7] R. Steinigeweg, J. Herbrych, and P. Prelovšek, *Eigenstate thermalization within isolated spin-chain systems*, Phys. Rev. E **87**, 012118 (2013).
[8] H. Kim, T. N. Ikeda, and D. A. Huse, *Testing whether all eigenstates obey the eigenstate thermalization hypothesis*, Phys. Rev. E **90**, 052105 (2014).
[9] W. Beugeling, R. Moessner, and M. Haque, *Finite-size scaling of eigenstate thermalization*, Phys. Rev. E **89**, 042112 (2014).
[10] W. Beugeling, R. Moessner, and M. Haque, *Off-diagonal matrix elements of local operators in many-body quantum systems*, Phys. Rev. E **91**, 012144 (2015).
[11] A. Chandran, M. D. Schulz, and F. J. Burnell, *The eigenstate thermalization hypothesis in constrained Hilbert spaces: A case study in non-Abelian anyon chains*, Phys. Rev. B **94**, 235122 (2016).
[12] R. Mondaini and M. Rigol, *Eigenstate thermalization in the two-dimensional transverse field Ising model. II. Off-diagonal matrix elements of observables*, Phys. Rev. E **96**, 012157 (2017).
[13] C. Nation and D. Porras, *Off-diagonal observable elements from random matrix theory: Distributions, Fluctuations, and Eigenstate Thermalization*, New J. Phys. **20**, 103003 (2018).
[14] T. Yoshizawa, E. Iyoda, and T. Sagawa, *Numerical large deviation analysis of the eigenstate thermalization hypothesis*, Phys. Rev. Lett. **120**, 200604 (2018).
[15] I. M. Khaymovich, M. Haque, and P. A. McClarty, *Eigenstate thermalization, random matrix theory, and behemoths*, Phys. Rev. Lett. **122**, 070601 (2019).
[16] S. Pappalardi, L. Foini, and J. Kurchan, *Eigenstate thermalization hypothesis and free probability*, Phys. Rev. Lett. **129**, 170603 (2022).
[17] G. Biroli, C. Kollath, and A. M. Läuchli, *Effect of rare fluctuations on the thermalization of isolated quantum systems*, Phys. Rev. Lett. **105**, 250401 (2010).
[18] T. N. Ikeda, Y. Watanabe, and M. Ueda, *Finite-size scaling analysis of the eigenstate thermalization hypothesis in a one-dimensional interacting Bose gas*, Phys. Rev. E **87**, 012125 (2013).
[19] V. Alba, *Eigenstate thermalization hypothesis and integrability in quantum spin chains*, Phys. Rev. B **91**, 155123 (2015).
[20] E. Khatami, G. Pupillo, M. Srednicki, and M. Rigol, *Fluctuation-dissipation theorem in an isolated system of*

quantum dipolar bosons after a quench, Phys. Rev. Lett. **111**, 050403 (2013).
[21] T. LeBlond, K. Mallayya, L. Vidmar, and M. Rigol, *Entanglement and matrix elements of observables in interacting integrable systems*, Phys. Rev. E **100**, 062134 (2019).
[22] M. Brenes, J. Goold, and M. Rigol, *Low-frequency behavior of off-diagonal matrix elements in the integrable XXZ chain and in a locally perturbed quantum-chaotic XXZ chain*, Phys. Rev. B **102**, 075127 (2020).
[23] T. LeBlond and M. Rigol, *Eigenstate thermalization for observables that break Hamiltonian symmetries and its counterpart in interacting integrable systems*, Phys. Rev. E **102**, 062113 (2020).
[24] M. Mierzejewski and L. Vidmar, *Quantitative impact of integrals of motion on the eigenstate thermalization hypothesis*, Phys. Rev. Lett. **124**, 040603 (2020).
[25] Y. Zhang, L. Vidmar, and M. Rigol, *Statistical properties of the off-diagonal matrix elements of observables in eigenstates of integrable systems*, Phys. Rev. E **106**, 014132 (2022).
[26] V. Korepin, N. Bogoliubov, and A. Izergin, *Quantum Inverse Scattering Method and Correlation Functions*, Cambridge Monographs on Mathematical Physics (Cambridge University Press, Cambridge, England, 1993).
[27] M. Takahashi, *Thermodynamics of One-Dimensional Solvable Models* (Cambridge University Press, Cambridge, England, 1999).
[28] F. H. L. Essler, H. Frahm, F. Göhmann, A. Klümper, and V. E. Korepin, *The One-Dimensional Hubbard Model* (Cambridge University Press, Cambridge, England, 2005).
[29] M. Gaudin, *The Bethe Wavefunction* (Cambridge University Press, Cambridge, England, 2014).
[30] F. A. Smirnov, *Form Factors in Completely Integrable Models of Quantum Field Theory*, Vol. 14 (World Scientific, Singapore, 1992).
[31] V. E. Korepin, *Calculation of norms of Bethe wave functions*, Commun. Math. Phys. **86**, 391 (1982).
[32] N. A. Slavnov, *Calculation of scalar products of wave functions and form factors in the framework of the algebraic Bethe ansatz*, Theor. Math. Phys. **79**, 502 (1989).
[33] J.-S. Caux, P. Calabrese, and N. A. Slavnov, *One-particle dynamical correlations in the one-dimensional Bose gas*, J. Stat. Mech. (2007) P01008.
[34] L. Piroli and P. Calabrese, *Exact formulas for the form factors of local operators in the Lieb–Liniger model*, J. Phys. A **48**, 454002 (2015).
[35] E. H. Lieb and W. Liniger, *Exact analysis of an interacting Bose gas. I. The general solution and the ground state*, Phys. Rev. **130**, 1605 (1963).
[36] H. Bethe, *Zur theorie der metalle: I. Eigenwerte und eigenfunktionen der linearen atomkette*, Z. Phys. **71**, 205 (1931) [, *On the theory of metals*, in *The Many-Body Problem: An Encyclopedia of Exactly Solved Models in One Dimension*, edited by (World Scientific, Singapore, 1993), ISBN 981-02-0975-4 (paperback: 981-02-1476-6)].
[37] I. Bloch, J. Dalibard, and W. Zwerger, *Many-body physics with ultracold gases*, Rev. Mod. Phys. **80**, 885 (2008).
[38] M. A. Cazalilla, R. Citro, T. Giamarchi, E. Orignac, and M. Rigol, *One dimensional bosons: From condensed matter systems to ultracold gases*, Rev. Mod. Phys. **83**, 1405 (2011).
[39] N. Kitanine, K. Kozlowski, J. M. Maillet, N. Slavnov, and V. Terras, *Form factor approach to dynamical correlation functions in critical models*, J. Stat. Mech. (2012) P09001.
[40] N. Fabbri, M. Panfil, D. Clément, L. Fallani, M. Inguscio, C. Fort, and J.-S. Caux, *Dynamical structure factor of one-dimensional Bose gases: Experimental signatures of beyond-Luttinger-liquid physics*, Phys. Rev. A **91**, 043617 (2015).
[41] F. Meinert, M. Panfil, M. J. Mark, K. Lauber, J.-S. Caux, and H.-C. Nägerl, *Probing the excitations of a Lieb-Liniger gas from weak to strong coupling*, Phys. Rev. Lett. **115**, 085301 (2015).
[42] K. K. Kozlowski, *Large-distance and long-time asymptotic behavior of the reduced density matrix in the non-linear Schrödinger model*, in *Annales Henri Poincaré*, Vol. 16 (Springer, New York, 2015), pp. 437–534.
[43] B. Doyon and H. Spohn, *Drude weight for the Lieb-Liniger Bose gas*, SciPost Phys. **3**, 039 (2017).
[44] B. Doyon, *Exact large-scale correlations in integrable systems out of equilibrium*, SciPost Phys. **5**, 54 (2018).
[45] E. Granet and F. H. L. Essler, *A systematic $1/c$-expansion of form factor sums for dynamical correlations in the Lieb-Liniger model*, SciPost Phys. **9**, 82 (2020).
[46] E. Granet, *Low-density limit of dynamical correlations in the Lieb–Liniger model*, J. Phys. A **54**, 154001 (2021).
[47] J.-S. Caux and F. H. L. Essler, *Time evolution of local observables after quenching to an integrable model*, Phys. Rev. Lett. **110**, 257203 (2013).
[48] M. Kormos, A. Shashi, Y.-Z. Chou, J.-S. Caux, and A. Imambekov, *Interaction quenches in the one-dimensional Bose gas*, Phys. Rev. B **88**, 205131 (2013).
[49] J. De Nardis, B. Wouters, M. Brockmann, and J.-S. Caux, *Solution for an interaction quench in the Lieb-Liniger Bose gas*, Phys. Rev. A **89**, 033601 (2014).
[50] M. Kormos, M. Collura, and P. Calabrese, *Analytic results for a quantum quench from free to hard-core one-dimensional bosons*, Phys. Rev. A **89**, 013609 (2014).
[51] J. De Nardis and M. Panfil, *Density form factors of the 1D Bose gas for finite entropy states*, J. Stat. Mech. (2015) P02019.
[52] L. Piroli, P. Calabrese, and F. H. L. Essler, *Multiparticle bound-state formation following a quantum quench to the one-dimensional Bose gas with attractive interactions*, Phys. Rev. Lett. **116**, 070408 (2016).
[53] I. Bouchoule and J. Dubail, *Generalized hydrodynamics in the one-dimensional Bose gas: Theory and experiments*, J. Stat. Mech. (2022) 014003.
[54] N. Robinson, A. de Klerk, and J.-S. Caux, *On computing non-equilibrium dynamics following a quench*, SciPost Phys. **11**, 104 (2021).
[55] E. Granet and F. H. L. Essler, *Systematic strong coupling expansion for out-of-equilibrium dynamics in the Lieb-Liniger model*, SciPost Phys. **11**, 68 (2021).
[56] F. H. L. Essler, *Applications of integrable models in condensed matter and cold atom physics*, in *Integrability: From Statistical Systems to Gauge Theory: Lecture Notes of the Les Houches Summer School* (Oxford Academic, Oxford, 2019), Vol. 106, p. 319, 10.1093/oso/9780198828150.003.0007.

[57] F. H. L. Essler, *A short introduction to generalized hydrodynamics*, Physica (Amsterdam) **631A**, 127572 (2022).
[58] D. B. Creamer, H. Thacker, and D. Wilkinson, *Quantum Gel'fand-Levitan method as a generalized Jordan-Wigner transformation*, Phys. Lett. B **92**, 144 (1980).
[59] M. Girardeau, *Relationship between systems of impenetrable bosons and fermions in one dimension*, J. Math. Phys. (N.Y.) **1**, 516 (1960).
[60] T. Veness, F. H. L. Essler, and M. P. A. Fisher, *Quantum disentangled liquid in the half-filled Hubbard model*, Phys. Rev. B **96**, 195153 (2017).
[61] J. De Nardis and M. Panfil, *Edge singularities and quasi-long-range order in nonequilibrium steady states*, Phys. Rev. Lett. **120**, 217206 (2018).
[62] B. Davies and V. E. Korepin, *Higher conservation laws for the quantum non-linear Schrödinger equation*, arXiv:1109.6604.
[63] S. Lukyanov, *Free field representation for massive integrable models*, Commun. Math. Phys. **167**, 183 (1995).
[64] F. H. L. Essler and M. Fagotti, *Quench dynamics and relaxation in isolated integrable quantum spin chains*, J. Stat. Mech. (2016) 064002.
[65] E. Granet, M. Fagotti, and F. H. L. Essler, *Finite temperature and quench dynamics in the transverse field Ising model from form factor expansions*, SciPost Phys. **9**, 033 (2020).
[66] P. Calabrese, F. H. L. Essler, and M. Fagotti, *Quantum quench in the transverse field Ising chain: I. Time evolution of order parameter correlators*, J. Stat. Mech. (2012) P07016.
[67] B. Bertini, D. Schuricht, and F. H. L. Essler, *Quantum quench in the sine-Gordon model*, J. Stat. Mech. (2014) P10035.
[68] D. Schuricht and F. H. L. Essler, *Dynamics in the Ising field theory after a quantum quench*, J. Stat. Mech. (2012) P04017.
[69] We note, however, that essentially equally good descriptions of the data are obtained by two-parameter fits to $f(x) = a_3 x^{a_4}$.
[70] F. H. L. Essler (unpublished).
[71] V. B. Bulchandani, D. A. Huse, and S. Gopalakrishnan, *Onset of many-body quantum chaos due to breaking integrability*, Phys. Rev. B **105**, 214308 (2022).